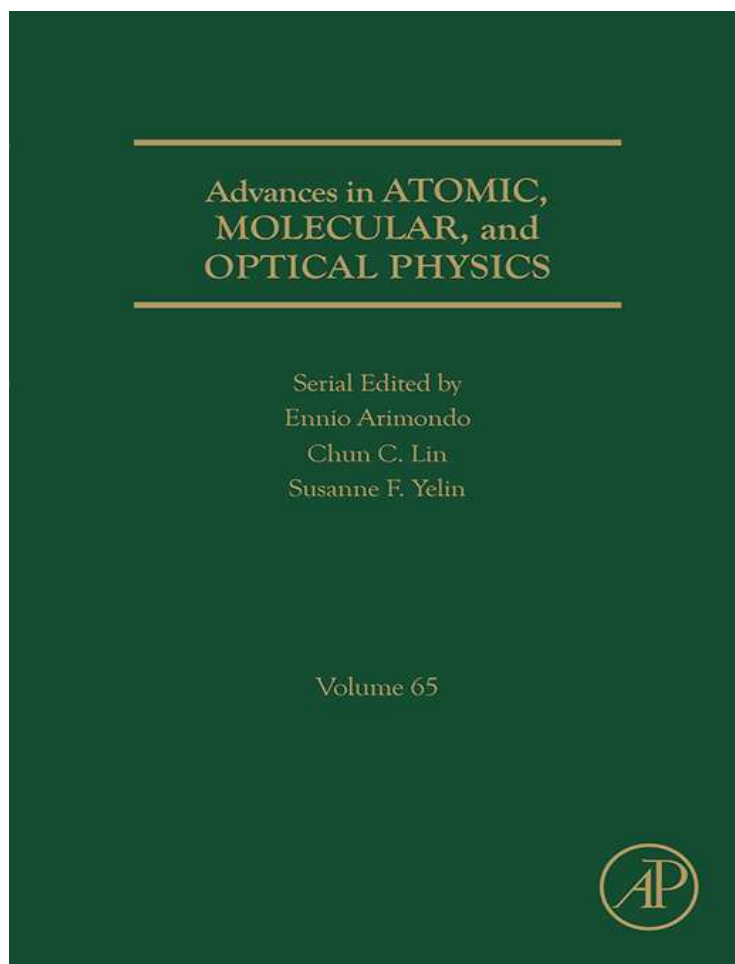


**Provided for non-commercial research and educational use only.
Not for reproduction, distribution or commercial use.**

This chapter was originally published in the book *Advances In Atomic, Molecular, and Optical Physics, Vol. 65* published by Elsevier, and the attached copy is provided by Elsevier for the author's benefit and for the benefit of the author's institution, for non-commercial research and educational use including without limitation use in instruction at your institution, sending it to specific colleagues who know you, and providing a copy to your institution's administrator.



All other uses, reproduction and distribution, including without limitation commercial reprints, selling or licensing copies or access, or posting on open internet sites, your personal or institution's website or repository, are prohibited. For exceptions, permission may be sought for such use through Elsevier's permissions site at:

<http://www.elsevier.com/locate/permissionusematerial>

From J.A.C. Gallas, Spiking Systematics in Some CO₂ Laser Models. In: Ennio Arimondo, Chun C. Lin and Susanne F. Yelin, editors, *Advances In Atomic, Molecular, and Optical Physics, Vol. 65*, Burlington: Academic Press, 2016, pp. 127-191.

ISBN: 978-0-12-804828-3

© Copyright 2016 Elsevier Inc.

Academic Press



Spiking Systematics in Some CO₂ Laser Models

J.A.C. Gallas¹

Instituto de Altos Estudos da Paraíba, João Pessoa, Brazil

Universidade Federal da Paraíba, João Pessoa, Brazil

Institute for Multiscale Simulations, Friedrich–Alexander Universität Erlangen–Nürnberg, Erlangen, Germany

Max–Planck Institute for the Physics of Complex Systems, Dresden, Germany

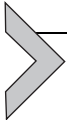
¹Corresponding author: e-mail address: jason.gallas@gmail.com

Contents

1. Introduction	128
2. Computation of Stability Charts	131
3. Spiking in Selected CO ₂ Laser Models	134
3.1 First Experimental Observation of Laser Chaos	134
3.2 CO ₂ with Feedback, Three-Dimensional Model	140
3.3 State of the Art: Six-Dimensional Model	151
3.4 Delayed Feedback, Infinite Dimension	170
4. Conclusions and Outlook	184
Acknowledgments	187
References	187

Abstract

The CO₂ laser is a complex dynamical system that has been investigated extensively both experimentally and through numerical simulations. As a result, a number of models exist for this laser, famed for providing satisfactory agreement between numerical and experimental observations. But the laser involves a large number of freely tunable control parameters whose impact on its performance and stability is not known in detail. The spontaneous emergence and organization of laser stability phases are also poorly understood. Here, we review recent progress in the classification of laser spiking, periodic or nonperiodic self-pulsations, predicted for CO₂ lasers with modulated parameters and with feedback, instantaneous or delayed. The unfolding of spiking is classified with the help of numerically obtained high-resolution stability charts for experimentally accessible control parameters. Such stability charts display novel regular and irregular features, suggesting that the laser control parameter planes harbor remarkable symmetries not yet accounted for theoretically but which are experimentally within reach. High-resolution stability charts put stringent tests on the reliability and accuracy of current models in forecasting laser dynamics.



1. INTRODUCTION

After establishing a laser model, the chief outstanding problem is the determination of its stability domains as a function of the control parameters. This problem is equivalent to the construction of phase diagrams for combinations of tunable parameters contained in the model. Traditionally, phase diagrams are constructed *analytically* following century-old recipes. They discriminate two basic types of solutions (Erneux and Glorieux, 2010): *fixed points*, ie, continuous-wave (CW) laser modes, and tame *oscillations*, namely time-varying solutions found after the so-called Hopf bifurcation boundaries, critical parameter boundaries beyond which fixed points are destabilized. Thus, analytically constructed phase diagrams normally consist of relatively simple curves discriminating parameters leading to nonoscillatory and oscillatory behaviors. Since models can be rather intricate, the fact that the curves are simple does not mean that their determination is simple. An additional complication of analytical works is that they frequently require introducing a number of approximations whose effect is not completely trivial to determine on the final expressions obtained. Recent advances in the theory of dynamical systems have shown that oscillatory modes can display an infinite number of distinct periodic wave patterns as well as a continuum of *chaotic* solutions, namely solutions where laser modes can display spikes and bursts without ever repeating. This calls for a classification of all sort of oscillatory laser modes.

Our goal is to provide an overview of current advances in the determination of laser stability charts. During recent years, interest in the structural organization of the control parameter plane of all sorts of lasers and other dynamical systems has been steadily increasing. Of primary interest are stability charts detailing how *stable* solutions self-organize themselves, or are organized by external forces, in parameter regions of interest of their normally high-dimensional control space. There is already extensive literature about laser phase diagrams, particularly for semiconductor lasers. For references see, eg, the surveys by Sciamanna and Shore (2015), Picozzi et al. (2014), Donati and Hwang (2012), and Wieczorek et al. (2005). Note, however, that in practical applications such diagrams are not as easy to use as one might have wished. The reason is that laser models are also playground for applied mathematicians looking for dynamically

intricate behaviors. Using continuation techniques, they normally obtain valuable diagrams which, however, combine phases corresponding to stable and unstable oscillations without a clear distinction between them. In contrast, here we focus on diagrams displaying only stable phases, which can be compared directly with experimentally obtained diagrams.

Broadly, this work reviews a number of recent findings concerning the distribution of self-pulsing in CO₂ lasers as a function of control parameters. The dynamics of the CO₂ laser (Patel, 1964; Zinth et al., 2011) was the subject of several investigations in recent years (Doedel and Pando, 2014; Doedel et al., 2014; Uchida et al., 2005). Of particular interest is to learn how to optimize the use of this powerful laser in applications and how to extract new theoretical insight from the knowledge of its dynamical characteristics. The reasons for the interest comes from applications such as, eg, coupling several lasers together to bypass the power limitations of individual lasers. Coupling lasers involves a plethora of new and unanticipated phenomena, for instance, the abundant emergence of random spiking and bursting, the synchronization of strongly pulsating lasers, and several other phenomena (Doedel et al., 2014; Larson et al., 2006; Susa et al., 2002; Uchida et al., 2005).

Specifically, the problem addressed here is the classification of laser oscillations and phases, sharing common characteristics of interest. As mentioned, the simplest possible stability phase is defined by the set of control parameters which produce stationary (CW) solutions. Next, there is an infinite number of phases corresponding to periodic oscillations with an arbitrarily high number of spikes per period. Finally, all nonperiodic oscillations form a third phase, the phase of chaos. Thus, the aforementioned classification problem amounts to determining the size and the boundaries for all phases, periodic or not.

Laser stability has been continuously a research subject ever since the laser invention. So, one may ask: what can be new about it? Briefly, fruitful and unanticipated novelties arise from the possibility of using computer clusters working at several petaflops, ie, with processing speeds of 10^{15} floating point operations per second, combined with terabytes of memory to perform systematic *numerical* investigation of arbitrary laser oscillations. Direct numerical simulations do not suffer from the aforementioned problems, due to approximations. As for discrete-time dynamical systems, numerical methods are nowadays reliable and can produce robust results for flows (continuous-time systems). For reliable models, numerical results agree with

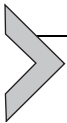
experiments and serve to gauge analytical approximations. The laser operation is normally described by rate equations and, accordingly, we consider state-of-the-art models currently used for CO₂ lasers.

Laser pulsations were already investigated for many situations of interest and are already summarized in books (Kane and Shore, 2005; Ohtsubo, 2013). A positive outcome of these investigations is that a satisfactory agreement was consistently reported between experiments and simulations. On the down side, such agreement usually holds for restricted set of parameters, covering no more than specific ad hoc values or intervals, motivated by specific applications. Thus, there is still a general lack of more encompassing and systematic analysis of the laser control parameters, classifying the nature and the relative abundance of stable pulsations. Why has this situation persisted thus far?

From an experimental point of view, the optimization of laser devices is a long-sought goal in quantum optics. In practice it is hard to achieve due to difficulties associated with continuously tuning parameters over extended ranges. Instead of efforts to better tune the performance of the lasers already known, the main emphasis has been to develop lasers to cover the full electromagnetic spectrum consistently with energy-efficient light sources like, eg, the energy-saving blue light-emitting diode whose discovery won the Nobel prize in 2014. Fortunately, detailed computer simulations can contribute now in several fronts to help optimize laser development and to design novel applications.

About 30 years ago, CO₂ lasers were used in pioneering experiments to verify phenomena and scenarios predicted in the then emergent field of nonlinear dynamics. The reason for using CO₂ lasers was its versatility and the relative handiness of its custom realization in well-equipped laboratories. Thus, the observation of deterministic chaos in CO₂ lasers with cavity modulation near the relaxation frequency was of primary importance (Arecchi et al., 1982a; Bonatto et al., 2005; Dangoisse et al., 1986, 1987; Lefranc and Glorieux, 1993; Zehnlé et al., 1992). From this experiment, other observations followed, confirming that chaos is also present in an autonomous configuration such as the CO₂ laser with optoelectronic feedback (Arecchi et al., 1986). Nowadays, applications involving optoelectronic and optical feedbacks in semiconductor lasers are widespread, specially in the field of secure communications, which rest on the phenomenon of chaotic synchronization between a master and a slave laser (Larson et al., 2006; Uchida et al., 2005).

To better understand the aforementioned phenomena in coupled lasers, an active field of research, one first needs a thorough understanding of a single CO₂ laser. The solitary laser involves a large number of freely tunable control parameters whose impact on its stability and performance, despite the large literature, has not yet been investigated. We review recent results that bridge this gap through a systematic numerical classification of complex dynamical phenomena observed in the CO₂. We also consider stability diagrams for easily accessible control parameters, and for parameters that are not so easily accessible, that imply more subtle changes of the physical characteristics of the laser medium.



2. COMPUTATION OF STABILITY CHARTS

The phase diagrams presented in several figures below were computed as follows. Any given two-parameter window of interest was divided into a discrete grid of equidistant points, usually $1200 \times 1200 = 1.44 \times 10^6$ points. Then, for each point, the equations of motion were integrated numerically using the standard fourth-order Runge–Kutta algorithm with fixed time step.

Laser stability is described here by three complementary types of stability diagrams: (i) the familiar stability diagram based on Lyapunov exponents (Argyris et al., 2015; Strogatz, 2015), (ii) stability diagrams displaying how the period of the oscillations evolves, and (iii) the so-called *isospike diagrams* (Freire and Gallas, 2011a,b; Gallas et al., 2014), based on counting the number of spikes contained in one period of the periodic oscillations. These three types of stability charts are illustrated in Fig. 1. As it is clear by comparing the panels in the three columns, all three types of diagrams provide the same basic information: they correctly discriminate chaos from periodicity. Note, however, that the isospike diagrams presented on the rightmost column are much more informative than the diagrams based on Lyapunov exponents and on the period of the oscillations: isospike diagrams not only discriminate periodicity from chaos but also indicate simultaneously where the number of spikes per period changes when parameters are tuned. They expose a lot of intricate structures in regions where the other domains show little or no variation at all. Below, we will use them frequently.

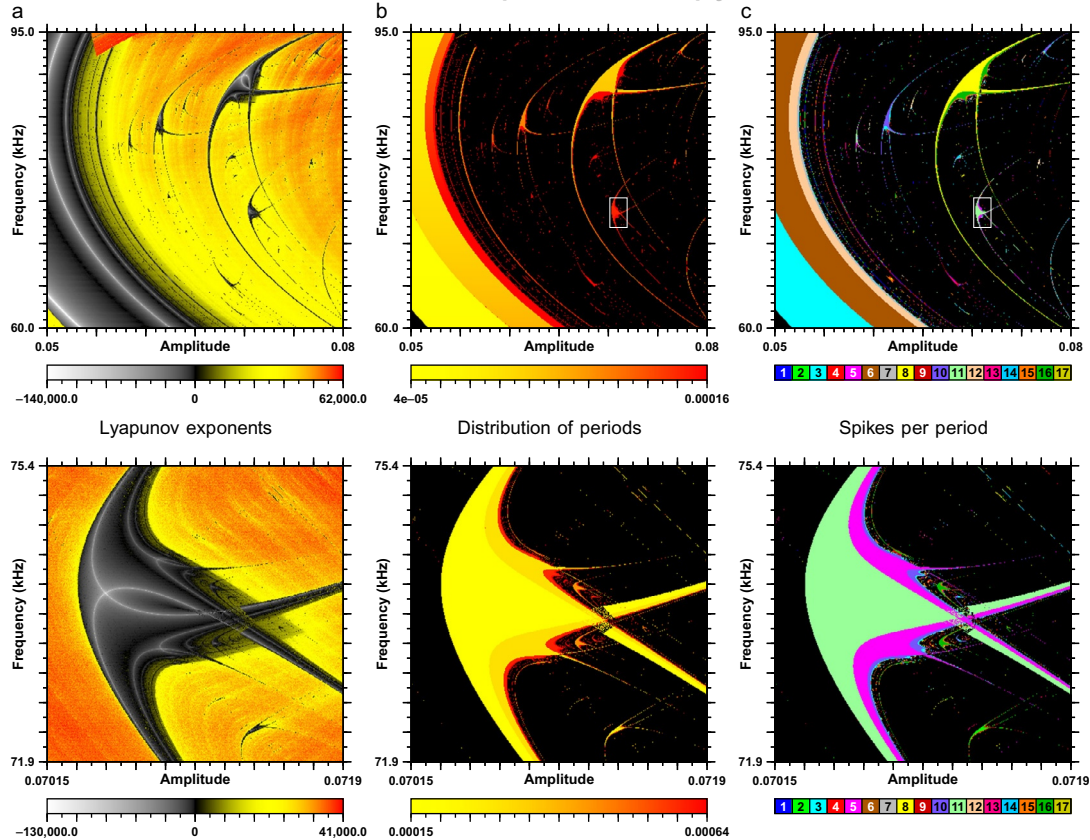
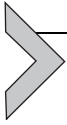


Fig. 1 Phase diagrams on the space of the frequency–amplitude variables describing laser self-pulsing for the CO₂ laser with modulated losses governed by Eqs. (1)–(3). The vertical columns show three distinct ways of representing the distribution of periodic and chaotic laser oscillations. The lower row are magnifications of the white box seen on two panels in the upper row. (a) Standard representation in terms of Lyapunov exponents. Positive exponents (indicated in colors (different gray shades in the print version)) represent chaotic oscillations. (b) Distribution of the period of the periodic oscillations. Lack of periodicity is shown in black. (c) Isospike diagram, showing the number of spikes per period. Aperiodicity shown in black. All three representations discriminate regularity from chaos, but isospikes are simpler to use because they do not require tuning scales in the control plane.

The diagrams in the center column represent the period of the pulses. They need to have the range of colors to be chosen manually by trial and error. This is so because the presence of high periods makes it difficult to find a good compromise for the range of colors that reveals the distribution of the smaller periods. In fact, the isospike diagrams on the rightmost column are valuable in helping to find suitable intervals to display the periods. In short, it is hard to automatize the selection of color ranges to better display variations of period.

When generating stability charts like [Fig. 1](#), integrations of the laser governing equations are normally done horizontally, moving from left to right, starting from an arbitrarily chosen initial condition and proceeding to the right by “following the attractor,” namely by using the values present in the computer buffer, at the end of a calculation for a given parameter, to start a new calculation after incrementing the parameter slightly horizontally. For details see, for example, [Freire et al. \(2009\)](#). In other words, instead of always reinitializing from the same initial conditions when changing parameters, we simply reused the conditions that were already stored in the computer buffer from a previous computation. This procedure was repeated for every parameter in the vertical axis. Normally, the first 2×10^5 integration steps were discarded as a transient time needed to approach the attractor. The subsequent 40×10^5 steps were then used to compute the Lyapunov spectrum, the period, and the number of spikes.

To obtain isospike diagrams, namely to find the number of spikes per period of the oscillations, subsequent to the computation of the Lyapunov exponents, we continued integrations for an additional 40×10^5 time steps recording up to 800 extrema (maxima and minima) of the variable of interest and checking whether pulses repeated or not. In the isospike diagrams we used a palette of 17 colors to represent the number of spikes contained in one period of the oscillations, as indicated by the colorbars in the figures. Patterns with more than 17 spikes are plotted by recycling the 17 basic colors modulo 17. Black represents “chaos” (ie, lack of numerically detectable periodicity), and white and orange colors mark nonoscillatory solutions, if any, having, respectively, nonzero or zero amplitudes of the variable under consideration. Isospike diagrams can be also efficiently implemented to deal with experimental data ([Sack et al., 2013](#)). The integration of differential equations for large sets of parameters and initial conditions is numerically a quite demanding task and can be performed only using computer clusters and suitable ad hoc programming.



3. SPIKING IN SELECTED CO₂ LASER MODELS

In this section, we discuss stability diagrams for some representative CO₂ laser models. The selected models involve low-dimensional models with or without modulated parameters, higher-dimensional models, and an infinite-dimensional model involving delayed feedback. The recurrent message is that these models display a rich variety of oscillatory modes and specific parameter combinations leading to unexpected behaviors.

3.1 First Experimental Observation of Laser Chaos

A technique used quite early to produce chaotic laser oscillations is by modulating control parameters of the so-called class B lasers (Arecchi et al., 1984). For instance, modulation of parameters was used in the influential work by Arecchi et al. (1982b), reporting measurements of subharmonic bifurcations, multistability, and chaotic behavior in a Q-switched CO₂ laser, a work that spurred a wide range of studies of parameter modulated lasers. Since then, modulated CO₂ lasers have been fruitfully exploited in many situations. Applications include studies of stochastic bifurcations in modulated CO₂ laser (Billings et al., 2004), multistability induced by periodic modulations (Chizhevsky, 2001), the rich response of CO₂ lasers with current modulation and cavity detuning (Pisarchik and Kuntsevich, 2001), and self-focusing effects in nematic liquid crystals (Brugioni and Meucci, 2004).

During the last 20 years, the CO₂ laser was extensively studied theoretically, numerically, and experimentally but focusing mainly on the characterization of dynamical behaviors in phase space (Hilborn, 2000; Ott, 2002; Strogatz, 2015) for specific parameters. Thus, while a detailed description of phase-space dynamics is available (Dangoisse et al., 1987; Gilmore, 1998; Gilmore and Lefranc, 2002; Tredicce et al., 1986), no comparable description exists for the parameter space. An exception is a work by Goswami (1994) who investigated analytically the first few period-doubling bifurcations for certain approximations of the Toda model of the CO₂ laser first described by Oppo and Politi (1985). Now, we describe features predicted by numerical simulations of the frequency–amplitude control space of a CO₂ laser with modulated losses. This serves to introduce a number of features of the control space that will appear again later, when discussing other laser models. For more details, see Bonatto et al. (2005) and references therein.

The simplest model of the single-mode dynamics of the loss-modulated CO₂ laser involves two coupled degrees of freedom governed by the equations for the dimensionless variables u and z (Arecchi et al., 1982b; Bonatto et al., 2005; Chizhevsky, 2001):

$$\frac{du}{dt} = \frac{1}{\tau} (z - k)u, \quad (1)$$

$$\frac{dz}{dt} = (z_0 - z)\gamma - uz. \quad (2)$$

Here, u is proportional to the radiation density, z and z_0 are the gain and unsaturated gain in the medium, respectively, τ denotes the transit time of the light in the laser cavity, γ is the gain decay rate, and $k \equiv k(t)$ represents the total cavity losses. The losses are modulated periodically and provide the third degree of freedom necessary for the system to support chaotic spiking:

$$k(t) = k_0(1 + a \cos 2\pi ft). \quad (3)$$

In this expression, k_0 represents the constant part of the losses, while a and f , the amplitude and frequency of the modulation, are the main bifurcation parameters of interest here. As frequently done (Bonatto et al., 2005; Chizhevsky, 2001), the remaining parameters are fixed at the realistic values $\tau = 3.5 \times 10^{-9}$ s, $\gamma = 1.978 \times 10^5$ s⁻¹, $z_0 = 0.175$, and $k_0 = 0.1731$.

Stability charts for this model are illustrated Figs. 1 and 2. A conspicuous feature in these figures are the so-called *shrimps* (Façanha et al., 2013; Gallas, 1993; Lorenz, 2008), seen at the center of the three panels on the bottom row of Fig. 1. As it may be recognized from the isospike diagrams on the rightmost column in Fig. 1, shrimps are complex structures composed by a doubly infinite succession of peak-doubling cascades of periodic oscillations plus a chaotic phase that follows them. As the number of spikes grows, they get more and more distorted as one sees in Fig. 2. A conspicuous feature observed as periodic laser pulses get more and more spikes is the regular self-organization of phases into a very regular network of self-similar shrimps. Such parameter space organization was previously known to exist in *discrete*-time dynamical systems (Gallas, 1993, 1995; Gallas and Nusse, 1996; Hunt et al., 1999). For flows, it was first observed by Bonatto et al. (2005) in a loss-modulated CO₂ laser.

Fig. 2a displays a global view of the parameter space. The most prominent features, the broad parabolic curved arcs in Fig. 2a, show that the

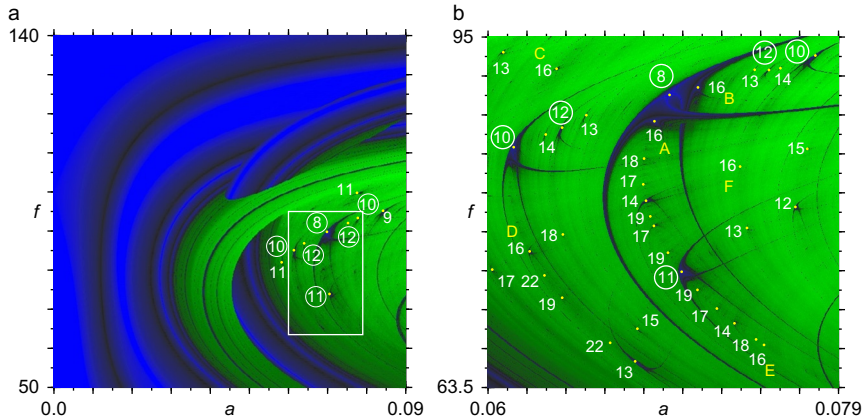


Fig. 2 Structure of the frequency–amplitude phase diagram of the laser showing a regular network of stability islands: (a) global view and (b) zoom of the box in (a). Numbers indicate the period of the laser intensity in multiples of 2π for each stability island; color intensities are proportional to Lyapunov exponents: blue (dark gray in the print version) for negative exponents (periodic oscillations), black for zero, and green (gray in the print version) for positive exponents (chaotic oscillations). Frequencies are in kHz.

control space of Eqs. (1) and (2) agrees well with the description found by Goswami (1994) for the Toda model of the CO₂ laser. For the parameters chosen, the relaxation frequency of the laser model is 50 kHz. In Fig. 2a one sees that there is a minimum amplitude threshold a beyond which subharmonic bifurcations start to occur, corresponding to a frequency about 100 kHz, the harmonic of the relaxation frequency (Bonatto et al., 2005). In addition, for certain parameter values new stability domains are created by saddle–node bifurcations, each of them undergoing then its own doubling cascades. In certain parameter ranges, more than one stable mode coexist (generalized multistability). This feature may be recognized in Fig. 2 from the sudden discontinuities in the coloring, which arise from the impossibility of plotting two distinct colors for the same parameter point.

A quite interesting feature in Fig. 2a is the remarkably regular structure inside the white box, magnified in Fig. 2b. This magnification shows that, embedded in the wide domain of parameters which lead to chaotic laser pulsations, there is a regular structure of self-similar parameter windows, shrimps, each one including infinite cascades of stable periodic oscillations. The period of the central region, “head,” of some of the larger shrimps is indicated by the number near to them, which denotes the period of the laser intensity in multiples of 2π .

In qualitative agreement with the organization of windows in Figs. 1 and 2, Pando et al. (1995) discovered that a four-level model of the laser behaves qualitatively similar to the prototypic Hénon map

$$x_{t+1} = a - x_t^2 + b y_t, \quad y_{t+1} = x_t. \quad (4)$$

In this discrete-time model, the parameter a (forcing) is taken as the bifurcation or control parameter. The damping parameter b varies between $-1 \leq b \leq 1$, the $b = 1$ representing the conservative limit and $b = 0$ the limit of strong damping. While for $b = 0$ (the logistic limit) there exists just a single attractor (distinct from $-\infty$) over a wide interval of a , when $b \neq 0$ one finds that several periodic and chaotic attractors may coexist. As for any class B laser, the CO₂ laser dynamics is characterized by a time delay between the intensity and the population inversion, a fact that nicely matches the delayed character of the Hénon map when written as a one-dimensional recurrence relation. Since it is easier to iterate maps than to integrate differential equations, it is interesting to compare what happens in the strongly dissipative limit of the map, focusing on slightly negative values of b .

Fig. 3 shows the regular self-organization of periodic pulsations along certain specific *directions* in the control space of the Hénon map obtained when starting on the left from the initial condition $(x_0, y_0) = (0.01, 0.01)$ and “following the attractor horizontally,” namely using the initial conditions stored in the computer buffer when updating parameters horizontally (Gallas, 2010). The ordering along the main diagonal of Fig. 3a is the same found for the laser, in Fig. 2a, along the direction containing the periods indicated inside circles. Similarly, the secondary diagonal in Fig. 3a displays the same ordering that the parabolic arc in the middle of Fig. 2c.

There is an excellent agreement between the laser and the Hénon map in phase space. This is corroborated by Fig. 4 which compares return maps between the laser (left column) and the Hénon map (right column). The laser return maps were constructed using the sequence $u_\ell(t)$, $\ell = 1, 2, 3, \dots$ of normalized relative maxima of $u(t)$. Another map displaying a similar organization and particularly suited to investigate analytically the inner structure of stability islands is the prototypical *canonical* quartic map $x_{t+1} = (x_t^2 - a)^2 - b$, introduced by Gallas (1993) and further discussed by Gallas (1994, 1995) and Hunt et al. (1999).

How easy is to detect experimentally the above regularities? Figure 5 illustrates a representative laser signal using two distinct vertical scales, linear and logarithmic. Although waveforms and underlying number of spikes

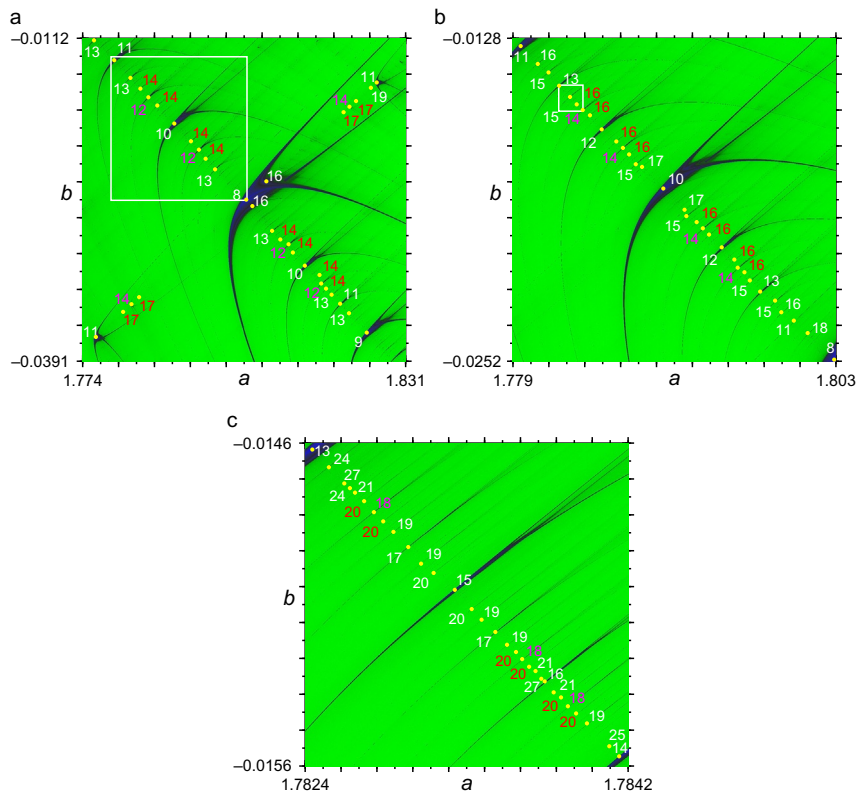


Fig. 3 The organization of the $a \times b$ parameter space of the Hénon map of Eq. (4) shown here mimics the organization found for the CO₂ laser but it is much easier to compute. (a) This shrimp organization coincides with the one of the laser, in Fig. 2b. The fine structure observed around period-8 here reproduces the laser period-8 sequence along the curve passing by the *encircled numbers* in Fig. 2b; (b) magnification of the box in (a); (c) magnification of the box in (b). Numbers indicate the main period of each stability island. Note the repetition of clustered patterns.

are easy to recognize in logarithmic scale, their experimental detection may become strenuous, particularly as the number of spikes increases. For instance, contemplating the six period-16 stability islands in Fig. 2b, one may ask what sort of differences distinguishes them and should be expected in their measurement. The answer is depicted in Fig. 6. In a real-world experiment, the difficulties to surmount are mainly to access narrow high-period windows and to have a detection range wide enough. Modulated losses are usually obtained with an intracavity polarizer and an electro-optical modulator. To detect large and small peaks simultaneously one can

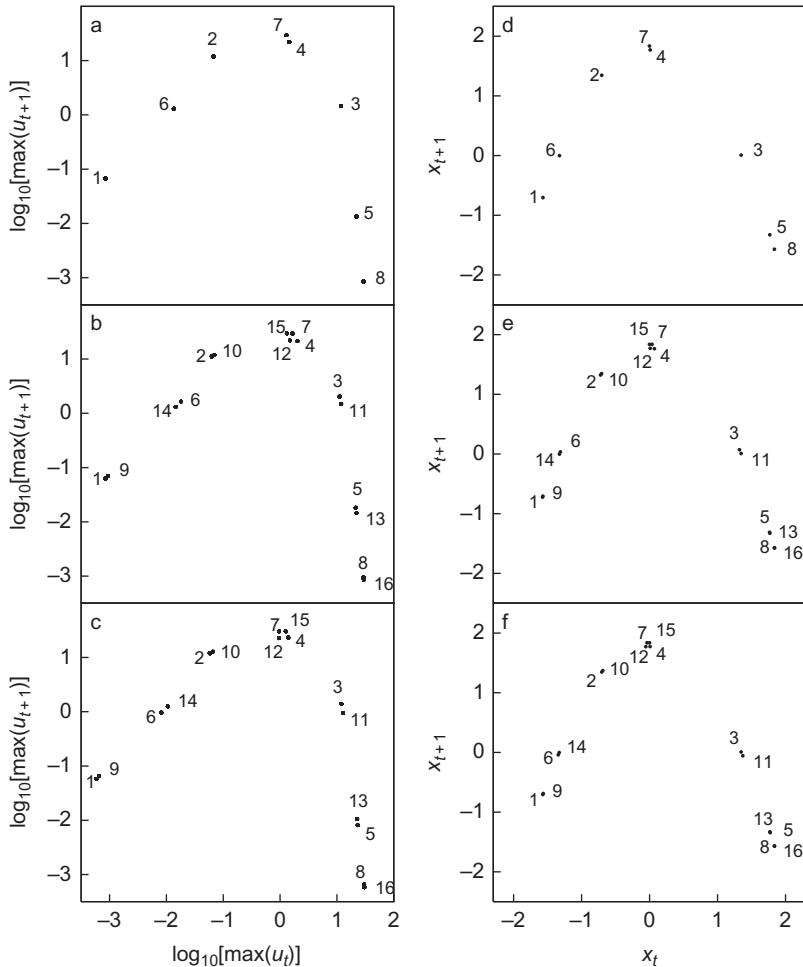


Fig. 4 Comparison of return maps for the CO₂ laser (left column) and the Hénon map (right column) illustrating the similarity of spiking, when (a) $(a, f) = (0.06984, 89.8)$, period-8; (b) $(0.07138, 90.47)$, period-16; (c) $(0.06902, 87.43)$, period-16. Frequencies are in kHz. Hénon return maps for period-8 and its doublings seen at the center of Fig. 3a, when (d) $(a, b) = (1.80287, -0.02514)$, period-8, (e) $(1.80395, -0.0257)$, period-16, (f) $(1.80642, -0.02356)$, period-16.

use a logarithmic preamplifier (Lefranc et al., 1992). Thus, experimental detection and discrimination of the laser signals in Fig. 6 are within reach with existing technology. Experimentally measured stability charts with high resolution have already appeared in the recent literature, but for electronic circuits (Sack et al., 2013), not lasers.

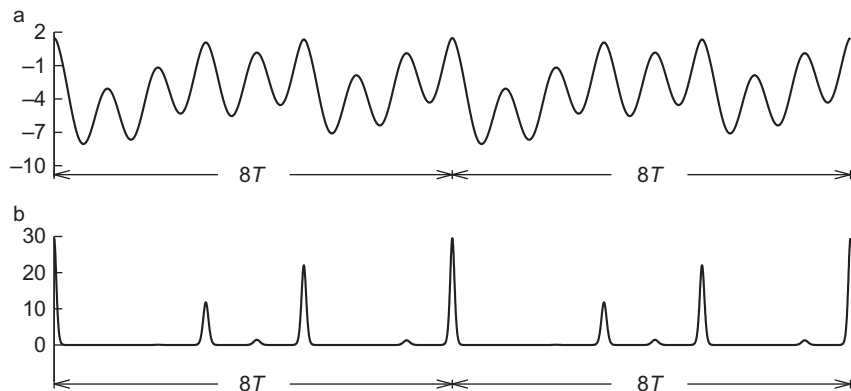


Fig. 5 Time evolution of the laser intensity $u(t)$ for the large period-8 structure in Fig. 2b, plotted in (a) logarithmic scale and (b) linear scale. Here $T = 1/(89.8 \text{ kHz})$ is the period of the modulation.

To uncover isomorphisms between the control space of flows (continuous-time systems) and maps (discrete-time) is important both from an applied and from a fundamental point of view. In this context, we mention results of Hunt et al. (1999) showing that for two-parameter systems there is a canonical family of quartic maps such that, typically, the bifurcations within a periodic window of a given scalar map are well approximated by linear transformations of the bifurcation diagram of the canonical quartic map. For practical applications, an important question is to investigate if parameter isomorphisms should be expected also for more refined laser models such as those discussed by, for example, Ciofini et al. (1993), Pando et al. (1993), and Meucci et al. (2004), which had not yet their control parameter space mapped systematically.

3.2 CO₂ with Feedback, Three-Dimensional Model

Next, we describe stability diagrams for a slightly more complicated system than before: a class B laser with optical feedback governed by a set of three rate equations (Arecchi et al., 1986; Junges and Gallas, 2012a; Vandermeiren et al., 2012; Wang et al., 1990; Yang et al., 1997). Feedback loops are standard ways of stabilizing and controlling the output frequency, wavelength and power of a laser, and the loop may involve optical, electronic, or electro-optical feedback (Fox et al., 2001). The efficient design of suitable feedback loops requires an understanding of the impact of parameter changes, informations which help optimize laser operation and further develop applications.

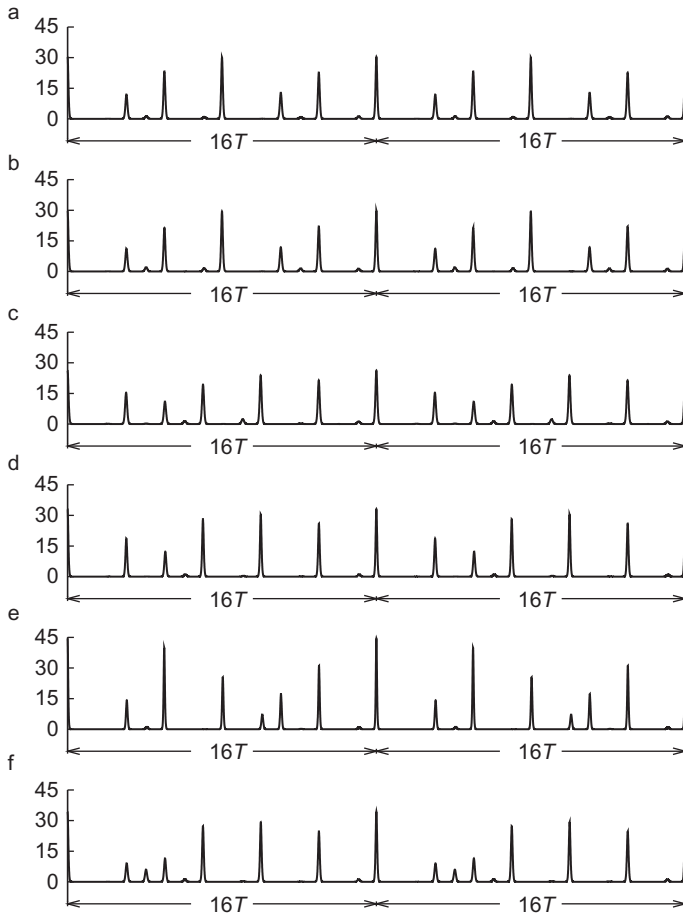


Fig. 6 Predicted time dependence of the laser intensity signals for the six period-16 stability islands labeled A, B, ..., F, in Fig. 2b. Signals (a) and (b), at points A and B, are period-8 doublings. All other signals are from islands which begin with period-16. Note that signals look very similar, despite the fact that they originate from very distinct regions of the parameter space. Parameters (a, f) are: (a) A = (0.06902, 87.43), (b) B = (0.07138, 90.47), (c) C = (0.063725, 92.15), (d) D = (0.062255, 75.735), (e) E = (0.0749617, 67.3281), (f) F = (0.073666, 83.359). The period $T = 1/f$ is different for each signal.

The model considered involves three variables and seven control parameters. Calling $x(t)$ the laser intensity normalized to the saturation value, $y(t)$ the population inversion normalized to the threshold value, and $z(t)$ the feedback voltage normalized to $1/\pi$ times the voltage of the electro-optic modulator, the governing equations can be written as

(Arecchi et al., 1986; Junges and Gallas, 2012a; Vandermeiren et al., 2012; Wang et al., 1990; Yang et al., 1997)

$$\dot{x} = kx(\gamma - 1 - \alpha \sin^2 z), \quad (5)$$

$$\dot{y} = \gamma(A - y - xy), \quad (6)$$

$$\dot{z} = \beta(B - rx - z). \quad (7)$$

In these equations, k stands for the unmodulated cavity loss, γ is the population decay rate, β is the damping rate of the feedback loop, r is the feedback gain, A is a normalized pump parameter, B is the bias voltage applied to an electro-optic modulator, and α is the amplitude of the modulation. As usual, B is normalized to $1/\pi$ times the half wavelength voltage of the modulator. Several of the earlier works either do not contain enough information that allow reproducing their results or contain inconsistencies preventing one from reproducing what they describe. An exception is the careful analysis of Yang et al. (1997), who focused on the $r \times B$ control plane for $A = 1.66$, $\alpha = 5.8$, $k = 9.6 \times 10^{-6} \text{ s}^{-1}$, $\gamma = 0.03 \times 10^{-6} \text{ s}^{-1}$, and $\beta = 0.5 \times 10^{-6} \text{ s}^{-1}$. Their realistic values are the same used here.

Yang et al. (1997) performed the standard linear stability analysis and identified stability boundaries between stable and unstable fixed-point (ie, nonoscillatory) solutions of the laser. They also computed numerically the period and the number of peaks per period of the laser intensity as a function of the parameters r (feedback gain) and B (bias voltage), defined in Eqs. (5)–(7). They observed that an increase in the feedback gain, r , results in an increase in the number of peaks of the laser intensity and found that an increase of the bias voltage, B , induces an increase in the period of the signal. They observed a divergence of the self-pulsing period T when increasing B after fixing r at a particular value, viz., $r = 0.21593$.

Fig. 7a and b presents $r \times B$ stability diagrams obtained by solving Eqs. (5)–(7) using a fixed-step $h = 0.002$ and starting integrations from $(x(0), y(0), z(0)) = (1, 1, 1)$. Using random initial conditions distributed uniformly in the interval $[0, 1]$ produces virtually identical diagrams. In these figures, fixed points (ie, nonoscillatory laser intensity) were plotted using two additional colors: the color of the large domain marked “constant non-zero laser intensity” in Fig. 1a, and white, to represent no-lasing solutions ($x = 0$). The no-lasing solutions appear as a very narrow white horizontal stripe at the top of Fig. 7a.

Fig. 7a and b illustrates how self-pulsations are distributed and organized in control parameter space. Fig. 7a displays a sequence of adjacent

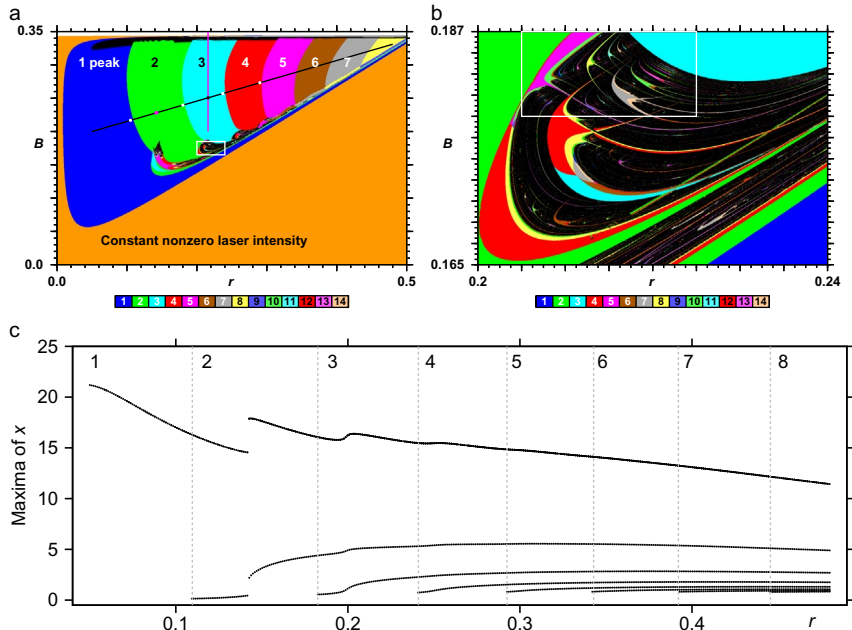


Fig. 7 (a) Stability diagram in the $r \times B$ plane classifying self-pulsating oscillations according to the number of peaks of the laser intensity, $x(t)$ in Eq. (5), as indicated by the numbers. Black denotes regions of chaotic oscillations. Black is also used in the horizontal stripe seen in the upper part of the figure to represent periods $T > 400$ (arbitrary units), ie, the divergence of the period. The narrow white stripe on the top marks zero intensity solutions (laser off). The points and pair of lines are discussed in subsequent figures (see text). (b) Magnification of the white box in (a) showing the same mosaic pattern reported recently for delay-differential equations (Junges and Gallas, 2012b) and standard accumulations of shrimps (see text). The box is shown magnified in Fig. 11b. (c) Bifurcation diagram showing the peak-adding cascade in $x(t)$ along the black line in (a), Eq. (8), as indicated by the numbers on the top of the figure. As described in the text, the laser intensity undergoes peak-adding cascades mediated by pulse deformations, not by windows of chaos, as usual. B and r are in the same units of [Arecchi et al. \(1986\)](#), [Wang et al. \(1990\)](#), [Yang et al. \(1997\)](#), and [Junges and Gallas \(2012a\)](#).

regions containing numbers denoting the number of peaks of the laser intensity. This organization agrees well with figure 3 of [Yang et al. \(1997\)](#) and extends it considerably, indicating that chaos is more abundant than originally found and that it recurs regularly in control parameter space. [Fig. 7b](#) presents details of the inner structure of one of the chaotic windows, the one inside the white box in [Fig. 7a](#), showing that laser phases have a quite complex organization, riddled by shrimp sequences ([Façanha et al., 2013](#); [Gallas, 1993](#); [Lorenz, 2008](#); [Oliveira and Leonel, 2011](#)),

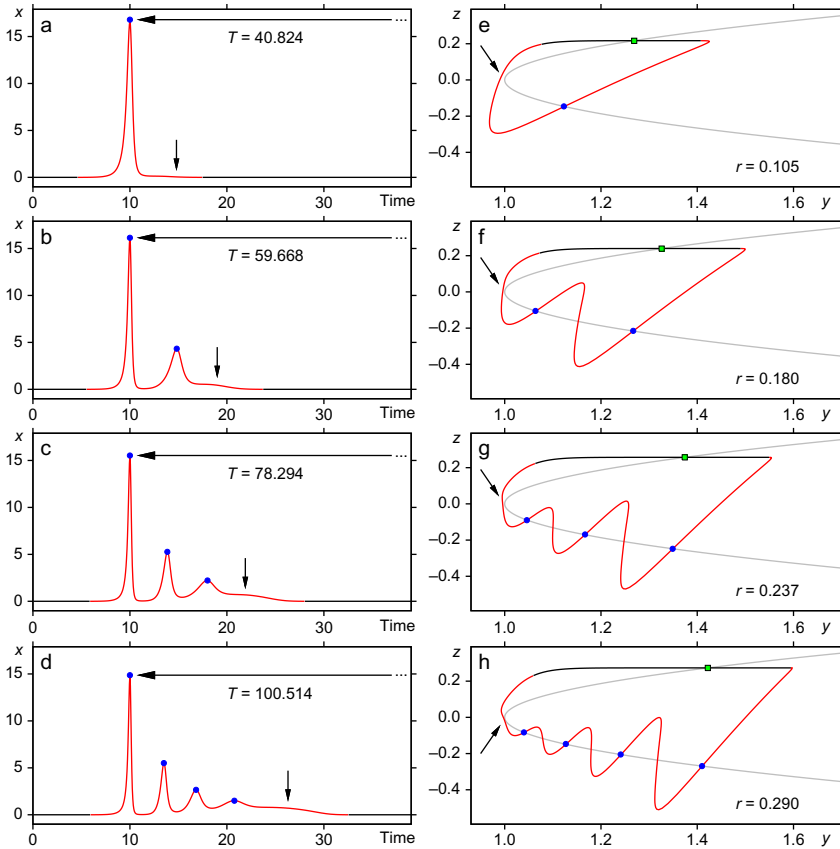


Fig. 8 (a–d) Laser self-pulsing $x(t)$ showing the increase in the number of peaks and intensity as r increases from $r = 0.105$ (top) to $r = 0.290$ (bottom), as indicated by the four white points along the black line in Fig. 7a. Vertical arrows mark the “precursor” of a new spike. (e–h) Intersections of undulated (y, z) red (gray in the print version) trace with the parabolic arcs $f(y, z) = 0$ (see text). Black segments of the undulated red (gray in the print version) trace denote laser off ($x < 0.005$). On all these plots, the arrows indicate the location of the intersections originating them. The green (gray in the print version) boxes mark the intersections of the laser-off segment of the trajectory with the curve $f(y, z) = 0$. It has no influence in dx/dt (see Eq. 5). Intersections seen between the blue (dark gray in the print version) dots mark local minima of the laser intensity. Note the fast increase of the self-pulsation period T . Time and periods are measured in μs .

namely by sequences of islands where we find periodic self-pulsations which unfold in a complex and specific way, via the pulse deformations described in Fig. 8. As may be seen from Fig. 7b, the control parameter space has specific boundaries where the shrimp sequences accumulate (Bonatto and Gallas, 2007).

The peculiar adjacent arrangement of isospike regions in Fig. 7a shows a subtle behavior, namely a peak-adding cascade where the number of peaks grows arithmetically, not geometrically as for the more frequently observed period-doubling cascade. More importantly, the several isospike windows are not separated by windows of chaos as it is more common for adding cascades (see Fig. 5) but, instead, here the number of peaks increases abruptly from window to window, without any trace of chaos between them.

Fig. 7a contains a black line, defined by the equation

$$B = 0.184756 + 0.304878 r, \quad 0.05 < r < 0.48. \quad (8)$$

Along this line we computed the bifurcation diagram shown in Fig. 7c, which illustrates in more detail how the number of peaks varies when two parameters are tuned simultaneously. Since the $x(t)$ varies continuously, to avoid plotting a solid black bar, the bifurcation diagram displays the local maxima of the laser intensity, each local maxima resulting in one branch of the bifurcation diagram. This bifurcation diagram is representative of the diagrams obtained along most lines of constant B , which display nothing else than more restricted views of the bifurcation cascade.

The bifurcation diagram in Fig. 7c is rather different from the more familiar ones, presenting a succession of *isolated branches*, namely single branches that start quite abruptly for specific values of r and evolve to form an atypical peak-adding cascade. This unfolding resembles what is known as mixed-mode oscillations (Freire and Gallas, 2011a), although here the unfolding is rather different, not mediated by chaos (Hauser and Gallas, 2014; Junges and Gallas, 2012a). Such isolated branches arise from *pulse deformations* when parameters evolve. Eq. (10) allows one to determine the emergence of new peaks in self-pulsations.

Fig. 8a–d displays examples of self-pulsations for $r = 0.105, 0.180, 0.237, 0.290$ and B as defined by Eq. (8). These four points are indicated by white dots on the black line in Fig. 7a. They are located immediately before the boundaries marking a change in the number of peaks of the laser intensity. Fig. 8a–d also contains a vertical arrow to indicate the location of a “precursor” of a peak, ie, the position where a new peak will arise when r is increased slightly. The explanation of the successive peak creation can be given referring to Fig. 8e–h, on the right column.

Fig. 8e–h shows two curves in the $y \times z$ plane. The first one, represented as a light parabolic arc, marks the solution of $f(y, z) = 0$, where

$$f(y, z) = y - 1 - \alpha \sin^2 z. \quad (9)$$

This function is an isocline defined by one of the two factors which appear in dx/dt (see Eq. 5). The other curve records the locus (y, z) obtained by integration of Eqs. (5)–(7).

The characteristic signature of the birth of a new isolated branch in the bifurcation diagram is the occurrence of *intersection points* between these two curves as parameters are tuned. The arrows in Fig. 8e–h show where new intersections will occur when r is increased slightly. Such intersections produce the several isolated branches at the bottom of the bifurcation diagram in Fig. 7c. Thus, the condition for the genesis of new peaks in self-pulsations or, equivalently, for new isolated branches in the bifurcation diagram is:

$$\frac{dx}{dt} = \frac{d^2x}{dt^2} = 0. \quad (10)$$

According to Eq. (5), this implies having

$$\frac{d^2x}{dt^2} = k \left[\frac{dx}{dt} f(y, z) + x \frac{df(y, z)}{dt} \right] = 0, \quad (11)$$

where $f(y, z)$ is given by Eq. (9). That this relation is indeed true can be verified numerically without difficulty. Clearly, the explicit conditions in Eq. (10) allows one to locate discontinuities in laser self-pulsations.

Summarizing from the peak-adding cascade in Fig. 8 one realizes the reason behind the emergence of extra peaks: they arise from continuous pulse deformations of the oscillations as the parameter varies. The isolated extra branches described here, arising from pulse deformations, should not be confused with discontinuous branches due to multistability. The latter involve discontinuous changes resulting from moving between *distinct* basins of attraction, while in the former self-pulsations evolve continuously staying always inside the *same* basin of attraction.

Discontinuities appear not only in the number of peaks (Fig. 7a) but also in the period (frequency) of the pulses and can be of two kinds. Fig. 9a presents a phase diagram showing how the period T varies as a function of the feedback gain r and bias voltage B . In this figure one easily recognizes two dark-green (black in the print version) regions, one horizontal, in the upper part of the diagram, and another one roughly parallel to the black line of Eq. (8). Two distinct kinds of discontinuities are observed when varying parameters along the pair of lines depicted in the figure.

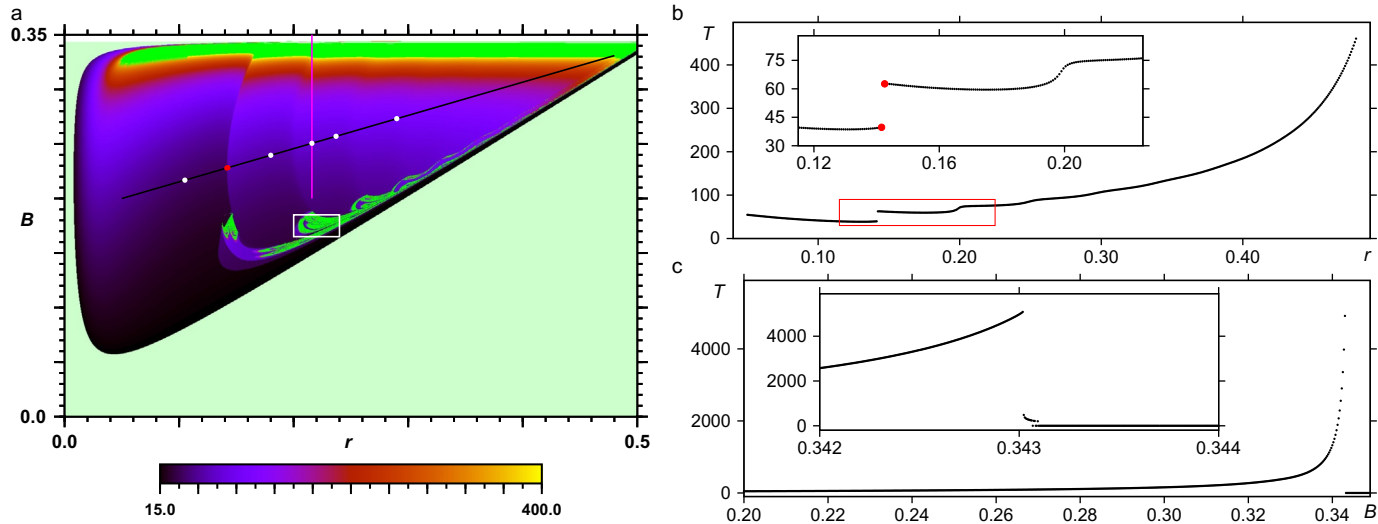


Fig. 9 (a) Stability diagram illustrating how the period T of $x(t)$ varies as a function of the r and B parameters. B and r are in the same units of [Arecchi et al. \(1986\)](#), [Wang et al. \(1990\)](#), [Yang et al. \(1997\)](#), and [Junges and Gallas \(2012a\)](#). There are several boundaries of discontinuous changes in the period. Along the *black line* in (a), the largest change is indicated by two (indistinguishable) *red (dark gray in the print version) dots*. (b) Variation of T (arbitrary units) along the *black line* in (a), showing a sharp jump of T near 0.14 and a smoother one near 0.20. Many other jumps exist, also when varying B , as indicated by the *vertical boundary bracketed by the red (gray in the print version) dots* in (a). (c) Variation of T along the *vertical red (light gray in the print version) line* at $r = 0.21593$ in (a) showing the divergence responsible for the *dark-green (black in the print version) horizontal stripe* in the upper part of that plot. (Note that after the divergence of the period there is a narrow region of finite period near $B = 0.343$. Multistability is also present in this region.)

The first type of discontinuity is shown in Fig. 9b which illustrates how the period evolves along the black line. The inset of this figure shows that a period discontinuity happens inside a very narrow interval, between $r = 0.1416$ and $r = 0.1426$. These values are plotted as red (dark gray in the print version) dots on the black line in Fig. 9a which, however, in the scale of the figure, are too close to each other to be distinguished as two distinct points. Between these dots one sees a curved vertical discontinuity boundary in the color coding, indicating a discontinuity in T . This boundary is characterized by jumps similar to the one shown in Fig. 9b. As this figure shows, additional discontinuities exist which, however, are much less pronounced and whose amplitudes decrease very rapidly.

A second type of discontinuity is shown in Fig. 9c and occurs along vertical lines, here $r = 0.21593$. This particular line was studied by Yang et al. (1997) who noted a *divergence* of T as B grows. Although the period can be calculated up to very high values, in Fig. 9a we introduced a cutoff at $T = 400$, considering all higher periods as divergences, ie, as lack of periodicity. This was done to magnify the visibility of the horizontal domain on the top of the figure. Actual divergences occur near the upper boundary of this domain. We stress, however, that the pair of dark-green (black in the print version) regions in Fig. 9a represent aperiodic pulses of a rather distinct nature. While the horizontal dark-green (black in the print version) stripe on the top of the figure marks *divergence of the pulse period*, the other region with a more complex shape, roughly parallel to the black line, marks *nonperiodic oscillations*, ie, chaotic laser pulses.

Comparing Fig. 9b and c one sees that the nature of the discontinuities along the black line display is much more complex than along the vertical line. Furthermore, comparison of Figs. 7a and 9a shows that discontinuities in the number of peaks do not coincide necessarily with discontinuities of the period, a fact clearly borne out in the two-peak window in the bifurcation diagram in Fig. 7c.

Using the same type of representation as in Fig. 8, Fig. 10 shows the cause of the discontinuous period jumps in Fig. 9b when passing between $r = 0.1416$ and $r = 0.1426$. Despite the fact that the red (gray in the print version) part of the trajectory (representing intervals where $x > 0$) in Fig. 10c to be larger than in Fig. 10d, they both correspond to an essentially identical lapse of time, as can be seen comparing the red (gray in the print version) segments in Fig. 10a and b. From these figures one may also recognize that in Fig. 10a the laser stays considerably longer with $x = 0$ than in Fig. 10b, what results in a sharp increase of the period. On the other hand, by

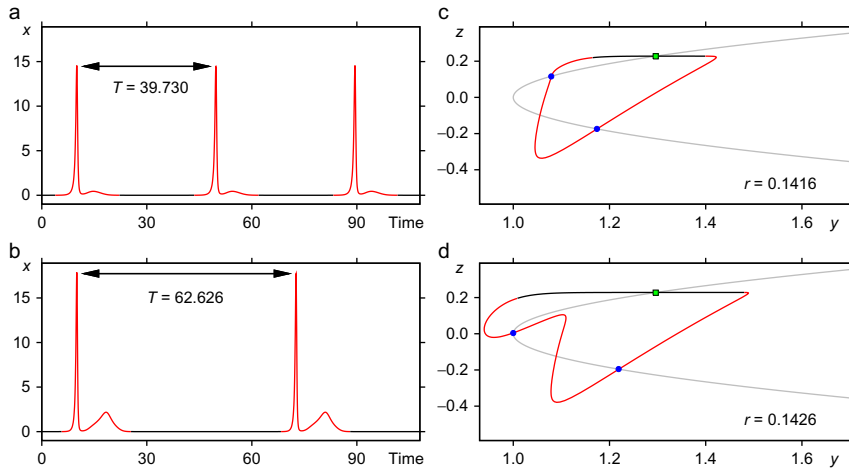


Fig. 10 Sudden increase in the period T of the time evolution of $x(t)$ (left column) and in the projections on the $y \times z$ plane (right column), induced by a very mild change of r , from $r = 0.1416$ (top row) to $r = 0.1426$ (bottom row). The jump in the period is due to the increase in the closed path, due to the added “undulation” seen in (d). The jump is similar to the ones described in Figs. 8 and 9. In both cases, before and after the jump, the laser pulse has two peaks per period. *Black segments and green (gray in the print version) boxes as in Fig. 8.* Time and period are measured in μs .

comparing the black segments in Fig. 10c and d we see an increase in the inversion y of the laser such that, when it decays, there is also an increase in the observed laser amplitude.

Fig. 11 shows details of the laser stability diagram for a parameter region dominated by chaotic self-pulsations. Fig. 11a uses Lyapunov exponents used to discriminate chaos (ie, positive exponents, shown in colors) from periodic pulses (negative exponents). As before, Lyapunov exponent stability agrees well with the phase diagram based on the number of peaks per period in Fig. 11b where colors emphasize periodic pulsations. Fig. 11b contains three white line segments along which bifurcation diagrams were computed, as shown on the left column. In the bifurcation diagram of Fig. 11c one sees a discontinuity in the number of peaks along the left-most line in Fig. 11b, similar to the discontinuities described earlier. However, the sequence of bifurcations along the two remaining line segments display peak-adding cascades of the more common type, namely cascades mediated by windows of chaotic pulses, observed previously in other systems (Bonatto and Gallas, 2008b; Bonatto et al., 2005). Note that the pair of peak-adding cascades converge toward a wide accumulation horizon (Bonatto and Gallas, 2007) characterized by pulses with three peaks, the

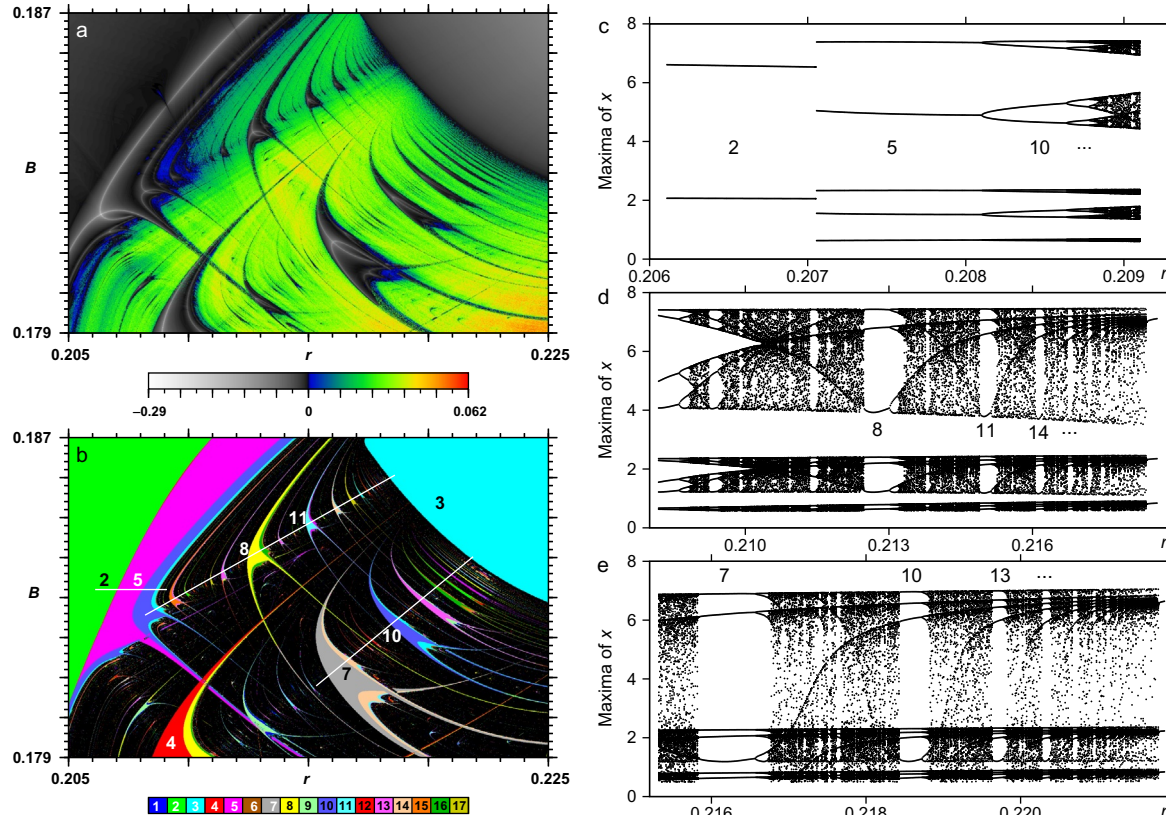


Fig. 11 Regular organization of stable self-pulsations in control plane. (a) Phase diagram of Lyapunov exponents in $r \times B$ plane, with colors (different gray shades in the print version) (associated to the Lyapunov exponent) emphasizing the extension of the chaotic phase. (b) Isospike phase diagram in $r \times B$ plane based on the number of peaks of the laser intensity, with colors (different gray shades in the print version) emphasizing periodicity islands. Along the pair of *nonhorizontal lines* one finds peak-adding shrimp cascades mediated by chaos. *Numbers* refer to the number of spikes in the laser intensity. (c–e) Bifurcations diagrams along the *three lines* shown in (b) showing the maxima of $x(t)$. Note that the pair of chaos-mediated peak-adding shrimp cascades occur along very particular “directions” (Gallas, 1993) and converge toward a large 3-spikes accumulation horizon (Bonatto and Gallas, 2007). In (b) colors (different gray shades in the print version) are recycled modulo 17. See text.

same number of pulses by which the cascades increase from shrimp to shrimp. This regular organization was observed before in several situations, eg, for an optically injected semiconductor laser (Bonatto and Gallas, 2007). Thus, while in some regions of the control space one observes novel *discontinuous* phenomena associated with pulse deformations, it is also possible to find wide regions where the organization is of the more common kind. The abrupt disruption of stability cascades by the new peaks arising from pulse deformations shows that, while stability phases may display identical shapes in control parameter space, the inner distribution of their pulses may be rather distinct displaying strong variations.

3.3 State of the Art: Six-Dimensional Model

In this section, we describe features observed in the control space of a six-dimensional model that is presently reputed as the best available to describe CO₂ lasers with feedback. It is defined by the equations for six dimensionless variables (Arecchi and Meucci, 2009; Ciofini et al., 1999; Freire et al., 2015; Pisarchik et al., 2001):

$$\dot{x}_1 = k_0 x_1 [x_2 - 1 - k_1 \sin^2(x_6)], \quad (12)$$

$$\dot{x}_2 = -\Gamma_1 x_2 - 2k_0 x_1 x_2 + \gamma x_3 + x_4 + P_0, \quad (13)$$

$$\dot{x}_3 = -\Gamma_1 x_3 + x_5 + \gamma x_2 + P_0, \quad (14)$$

$$\dot{x}_4 = -\Gamma_2 x_4 + \gamma x_5 + z x_2 + z P_0, \quad (15)$$

$$\dot{x}_5 = -\Gamma_2 x_5 + z x_3 + \gamma x_4 + z P_0, \quad (16)$$

$$\dot{x}_6 = \beta \left(B_0 - x_6 - \frac{R x_1}{1 + \alpha x_1} \right). \quad (17)$$

Here, x_1 represents the laser output intensity, x_2 the population inversion between the two resonant levels, and x_6 the feedback voltage signal which controls the cavity losses. These three coupled variables, equivalent to the (x, y, z) variables of Eqs. (5)–(7), are sufficient to generate chaos. However, due to the interplay of the different energy levels of the CO₂ molecule, one must introduce three additional variables acting as linear filters, increasing the overall dimension of the phase space from three to six. The variables x_3 , x_4 , and x_5 account for exchanges between the two molecular levels resonant with the radiation field and the other rotational levels of the same vibrational band of the molecule. The parameter k_0 controls the unperturbed cavity loss, k_1 determines the modulation strength, γ is a constant controlling the coupling between the subsystems (x_1, x_2, x_6) and (x_3, x_4, x_5) , Γ_1 and Γ_2 are population relaxation rates, P_0 the pump parameter

(related to the population inversion), and z represents the effective number of rotational levels. β, B_0, R, α are, respectively, the bandwidth, the bias voltage, the amplification, and the saturation factors of the feedback loop. Following [Pisarchik et al. \(2001\)](#) and [Freire et al. \(2015\)](#), we fix $\Gamma_1 = 10.0643$, $\Gamma_2 = 1.0643$, $\alpha = 32.8767$, $\beta = 0.4286$, $k_0 = 28.5714$, $k_1 = 4.5556$, $z = 10$, $\gamma = 0.05$, $R = 160$, $B_0 = 0.1026$, and $P_0 = 0.016$, all of them in dimensionless units. In all phase diagrams below, integrations were performed horizontally from left to right starting from an arbitrarily chosen initial condition, $(x_1, x_2, x_3, x_4, x_5, x_6) = (0.0011, 1.01, 1.05, 10.05, 10.3, 0)$, and proceeding by “following the attractor” ([Freire et al., 2015](#)). The first 2×10^5 integration steps were disregarded as a transient time needed to approach the attractor, with the subsequent 40×10^5 steps used to compute the Lyapunov spectrum, the period, and the number of spikes per period. A Lyapunov phase diagram for a reduced region of the $R \times B_0$ control space of this model was already given in figure 5c of [Bonatto and Gallas \(2008a\)](#). Larger and more detailed views of the $R \times B_0$ control plane are presented in [Figs. 12](#) and [13](#). Before presenting results for this and for other control planes, we first review significant steps that led to the model earlier.

3.3.1 Genesis of the Six-Dimensional Model

As already mentioned, the simplest approach to model the dynamics of a single-mode homogeneously broadened CO₂ laser is by using two rate equations, one for the laser intensity and the other for the population inversion between the two resonant levels. This description is appropriate for a class B laser, in the classification introduced by [Arecchi et al. \(1984\)](#). The two-level model was used to interpret the chaotic dynamics emerging in this kind of laser when an electro-optic feedback is introduced. When complemented by a third equation describing the optoelectronic feedback, the two-level laser equations provide the basic three-dimensional model necessary to foresee local bifurcations leading to chaos after the destabilization of a limit cycle ([Arecchi et al., 1986](#)) and global bifurcations related to the presence of a homoclinic connection in the phase space ([Arecchi et al., 1987](#)). This work argued to be possible to observe competing instabilities by operating a CO₂ laser with feedback in a parameter range with coexisting unstable fixed points. From local chaos originated around a stationary solution with nonzero laser output intensity (named solution “1”) it is possible to observe a transition to homoclinic chaos of the Shilnikov type around an apparent saddle focus (named solution “2”). In this regime, the trajectories

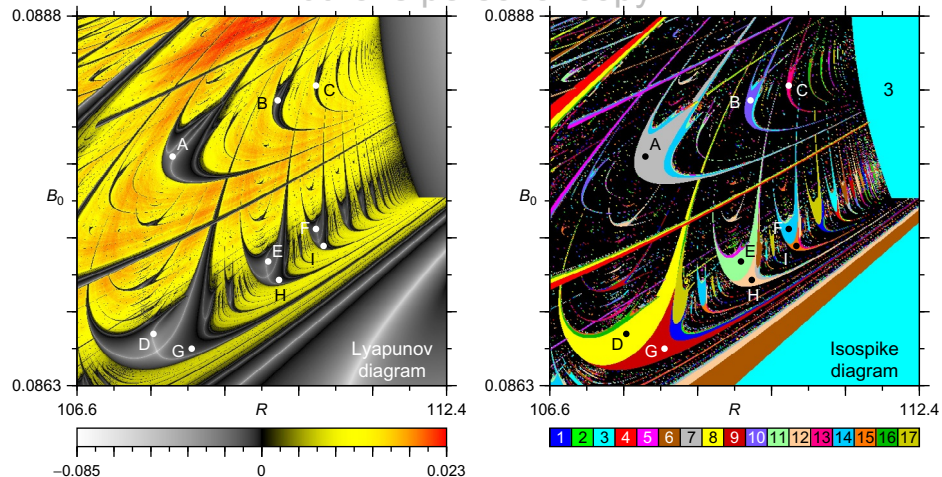


Fig. 12 The two panels on the top row two alternative representations of the laser stability as a function of the feedback gain R and bias voltage B_0 . Top left: standard Lyapunov stability diagram (Bonatto et al., 2005), where gray shadings mark periodic oscillations (negative value exponents), and colors (different gray shades in the print version) denote chaos (positive value exponents). Top right: isospike diagrams (see text), where colors (different gray shades in the print version) display the number of spikes in one period of the laser intensity x_1 and black denotes chaos (ie, lack of numerically detectable periodicity). The isospike diagram contains by far much more information than the Lyapunov diagram. The number 3 marks the domain toward which both 3-spikes adding cascades accumulate. (a–i) Temporal evolutions of intensity pulses for selected parameters, indicated by labeled dots in both top diagrams. The oscillation periods T_ℓ are given in the text. Black arrows in (g)–(i) indicate where new peaks are born (see text). For convenience, the vertical axis shows $10^3 x_1$.

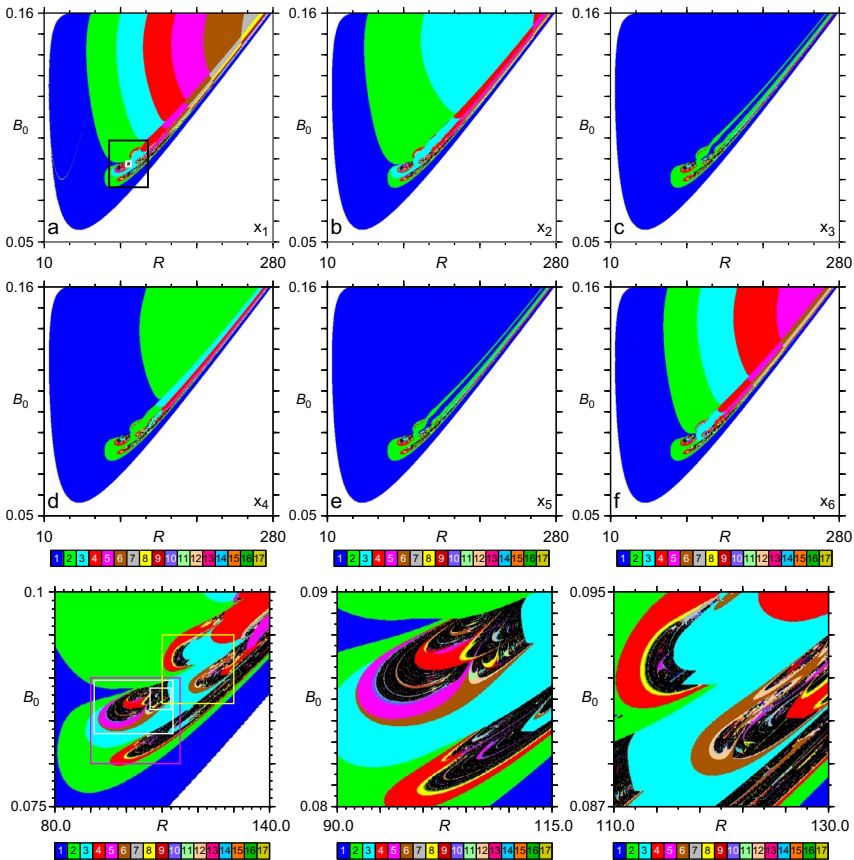


Fig. 13 Distribution of spikes in the $R \times B_0$ plane as a function of the six dynamical variables used to count the spikes in one period of (a) $x_1(t)$, (b) $x_2(t)$, (c) $x_3(t)$, (d) $x_4(t)$, (e) $x_5(t)$, and (f) $x_6(t)$. Black represents chaos (ie, nonperiodic spiking). White marks a region of constant but nonzero continuous wave laser intensities. In (a), the *small white rectangle* at the center of the *black box* marks the region enlarged in Fig. 1. Chaotic laser spiking is confined to comparatively small regions. Note the similarity of (a) and Fig. 7a obtained for the much simpler three-dimensional model. On the bottom row, the two rightmost panels show magnifications of the regions delimited by the *two largest boxes* inside the leftmost panel. The *two additional smaller boxes* contained in the leftmost panel are shown magnified in Fig. 12.

also visit the unstable solution with zero laser output intensity (named solution “0”). The situation is described in detail by [Arecchi et al. \(1987\)](#). Subsequent investigations revealed that it is not possible to find a stationary solution associated with this apparent saddle focus. This subtle and intriguing aspect in the global dynamics led to the investigation in more detail of the

Q-switching dynamics of the CO₂ laser related to the build-up process of the laser intensity originating from a spontaneous emission process when the laser is below threshold. Such analysis revealed that the two-level model is not adequate to fit experimental observations. To overcome this difficulty, a four-level model was introduced. Such model accounts for nonradiative couplings of the two resonant levels of the vibrational bands to which they belong. A precise description of the passive Q-switching in a CO₂ laser with intracavity saturable absorbers was given in Duprè et al. (1975), Arimondo et al. (1983), and Asquini and Casagrande (1983). Such a configuration also led to the observation of homoclinic chaos (Alcantara et al., 1995; Dangoisse et al., 1988; Erneux and Glorieux, 2010; Liu et al., 1994; Tachikawa et al., 1988; Zeni et al., 1993). The CO₂ laser with saturable absorber is *equivalent* to the CO₂ laser with feedback in the sense that homoclinic chaos is observed in both of them.

The transient behavior in CO₂ lasers with slowly swept parameters around the laser threshold was later explained by the four-level model with equal relaxation rates for the two vibrational bands (Arecchi et al., 1988). In this experiment, the features of the relaxation oscillations affecting the laser intensity after the crossing of the laser threshold have been characterized depending on the sweep rate of the cavity losses. Exploring laser dynamics near the laser threshold, another feature appears when the pump parameter is slowly swept, that is, the presence of a delayed bifurcation. Such a phenomenon, theoretically foreseen by Mandel and Erneux (2003), was experimentally observed and correctly explained by the four-level model for the CO₂ laser (Arecchi et al., 1989).

The analysis of the dynamical behavior of a Q-switched CO₂ laser revealed that the laser intensity in the nonlinear amplification regime and the long time relaxation process to the steady state are correctly explained only by using the four-level model with different relaxation rates of the two vibrational bands (Meucci et al., 1992). On the other hand, in the linear amplification regime both models produce the same result. In the case of chaotic dynamics obtained by means of sinusoidal modulation of cavity losses or by optoelectronic feedback the same considerations are still valid reinforcing the adequacy of the four-level model. The four-level model for the CO₂ laser consists of five differential equations involving the laser intensity I , the population of the lasing levels N_1 and N_2 , and the global population of the rotational manifolds M_1 and M_2 . Consequently the dynamics of a CO₂ laser with electro-optic feedback is ruled by a set of six differential equations (six-dimensional model). From a theoretical point of view, the

validity of the four-level model was demonstrated by a global application of center manifold theory allowing the reduction of the number of variables from six to four (Varone et al., 1995).

Successive experimental confirmations of the adequacy of the six-dimensional model are reported in Meucci et al. (1997), where evidence of stabilization of periodic solutions embedded in the chaotic attractor of this system is provided. The adopted strategy to control chaos is based on the introduction of an additional feedback loop where a selective filtering of the subharmonic components present in the chaotic laser intensity signal is performed. The final result of this filtering process is the rejection of the undesired subharmonic components responsible for chaos and the enhancement of the fundamental frequency component associated with the limit cycle stabilized in the phase space. This control method has been demonstrated particularly suitable for low-dimensional chaotic systems where it is possible, from a preliminary learning session, to extract the information necessary for selective filtering in the frequency domain. The six-dimensional model not only yields the unperturbed chaotic dynamics, but it is also crucial to describe its control. Control is implemented by adding the extra degrees of freedom related to the selective filtering. Although in this experiment one only considers local dynamical aspects of chaos, the six-dimensional model maintains its validity also when homoclinic chaos is directed to the fixed point (saddle focus) in the phase space (Ciofini et al., 1999).

Another class of experiments, exploring the role of chaotic synchronization induced by a sinusoidal forcing or by noise added in the feedback loop, drew attention to the high susceptibility of the system in the vicinity of the saddle focus (Allaria et al., 2001). As a small perturbation, including noise, is able to modify the global dynamics from chaos to periodicity and vice versa, synchronization can be easily obtained in a chain of CO₂ lasers in the homoclinic regime with nearest neighbor coupling (Arecchi et al., 2003; Leyva et al., 2003). For further details, see Freire et al. (2015).

3.3.2 Stability Charts

We start by comparing in Fig. 12 two types of stability diagrams for the six-dimensional model: the standard Lyapunov stability diagram and the isospike stability diagram based on counting the number of spikes per period (Freire and Gallas, 2011a,b; Freire et al., 2012; Gallas et al., 2014; Hauser and Gallas, 2014; Hoff et al., 2014; Sack et al., 2013). They are plotted as a function of the parameters studied most frequently in the literature, namely as a function of the feedback gain R and the bias voltage B_0 . The Lyapunov

diagram is shown on the leftmost top panel of Fig. 12. Gray shadings represent periodic oscillations (ie, negative exponents), while the colors denote chaos (ie, positive values of the exponents). A similar Lyapunov stability diagram showing a smaller stability region and slightly distinct parameter values was given in figure 5c of Bonatto and Gallas (2008a). In contrast, the rightmost panel shows the corresponding isospike diagram, which contains much more information. While both diagrams clearly discriminate regular from chaotic oscillations, the isospike diagram also informs how and where the complexification of the laser signal occurs, ie, it shows how to tune parameters in order to obtain more and more spikes in the laser oscillation via continuous deformations that create and destroy peaks, as described in the previous section for the three-dimensional model of a CO₂ laser with feedback (Junges and Gallas, 2012a), and also for the infinite-dimensional Mackey–Glass delayed feedback system (Junges and Gallas, 2012b).

On the top row of Fig. 12, both panels contain triplets of dots labeled (A, B, C), (D, E, F), and (G, H, I). Such points are the first ones of an infinite sequence of analogous points lying inside certain complex structures, denoted shrimps (Bonatto and Gallas, 2008a; Bonatto et al., 2005; Gallas, 1993, 1994; Gallas et al., 2014; Lorenz, 2008). These sequences of points accumulate toward a large region on the right-hand-side containing the number 3 (rightmost diagram on the top row) and representing periodic laser oscillations with 3–spikes per period. Panels (a)–(i) on the bottom of Fig. 12 show how the laser signal dependent on time changes along the first three of the infinite sequences of points. The period T_ℓ (arbitrary units) seems to grow continuously

$$(T_A, T_B, T_C, \dots) = (213.57, 300.32, 386.03, \dots), \quad (18)$$

$$(T_D, T_E, T_F, \dots) = (242.70, 327.61, 411.98, \dots), \quad (19)$$

$$(T_G, T_H, T_I, \dots) = (245.91, 329.97, 414.10, \dots). \quad (20)$$

But the number of spikes shows a remarkable behavior: While the number of spikes covers uniformly the main body of the shrimps forming the sequence A, B, C, ..., the main body of the sequences D, E, F, ... and G, H, I, ... are split into two separate domains characterized by distinct number of spikes. Uniform accumulations of spikes were observed before (Bonatto and Gallas, 2008a). But, as far as we know, shrimps containing double accumulations like the sequences D, E, F, ... and G, H, I, ... have not been observed before. Note that all the three spike-adding

accumulations involve the addition of three spikes, which is the number of spikes of the domain toward which they accumulate very fast.

The time evolutions in Fig. 12a–i suggest regularities in the steady complexification of laser patterns: Each family seems to be a concatenation of a few fixed combinations of quasi-identical patterns where the rightmost end of the wave pattern gets more and more extra spikes as one moves toward the accumulation boundary. This situation is reminiscent of behavior found recently in the Mackey–Glass delayed feedback system (Junges and Gallas, 2012b), a mathematically more complicated system, involving an infinite-dimensional set of equations.

Since we consider a six-dimensional model for the laser, a natural question to ask is whether or not the distribution of spikes depends on the specific dynamical variable used to count them. To check this, Fig. 13 presents six stability diagrams, one for each variable x_ℓ . This figure shows unambiguously that the recorded spikes distribution depends strongly on the variable used. It is also clear that the boundaries of the spiking phases lie in different positions. Curiously, the spiking phases seem to roughly organize themselves into three *similarity classes*, in the sense that each pair of variables (x_1, x_6) , (x_2, x_4) , and (x_3, x_5) produces a somewhat similar distribution of spikes. It is also manifest that the diagrams obtained for the variables (x_2, x_4) somewhat *interpolate* the diagrams obtained for the pairs (x_1, x_6) and (x_3, x_5) . It is noteworthy here that while x_1 (the laser output), x_2 (the population inversion), and x_6 (the feedback voltage) are more easy to be accessed experimentally, the remaining triplet x_3, x_4, x_5 , accounting for exchanges between the molecular levels resonant with the radiation and other rotational levels within the same vibrational band, is not directly accessible to experimentation.

Fig. 13 depicts a much larger region of the laser control space than the one shown in Fig. 12 and shows that the complexification of the laser intensity occurs via *nonchaos-mediated mixed-mode oscillations* (Hauser and Gallas, 2014). Another important piece of information provided by Fig. 2 is that periodic spiking (represented by nonblack phases) is by far the dominant behavior in this control plane of the laser. In other words, the black color representing chaos and seen extensively in Fig. 12, in fact exists only in comparatively small regions of this control space. As illustrated in Figs. 13 and 14 and in other similar figures below, this statement remains true for other sections of the control space.

How does the distribution of spikes looks like when recorded in other control parameter planes of the laser? This question is answered in the next few figures, obtained by counting spikes of the laser intensity x_1 . Fig. 14

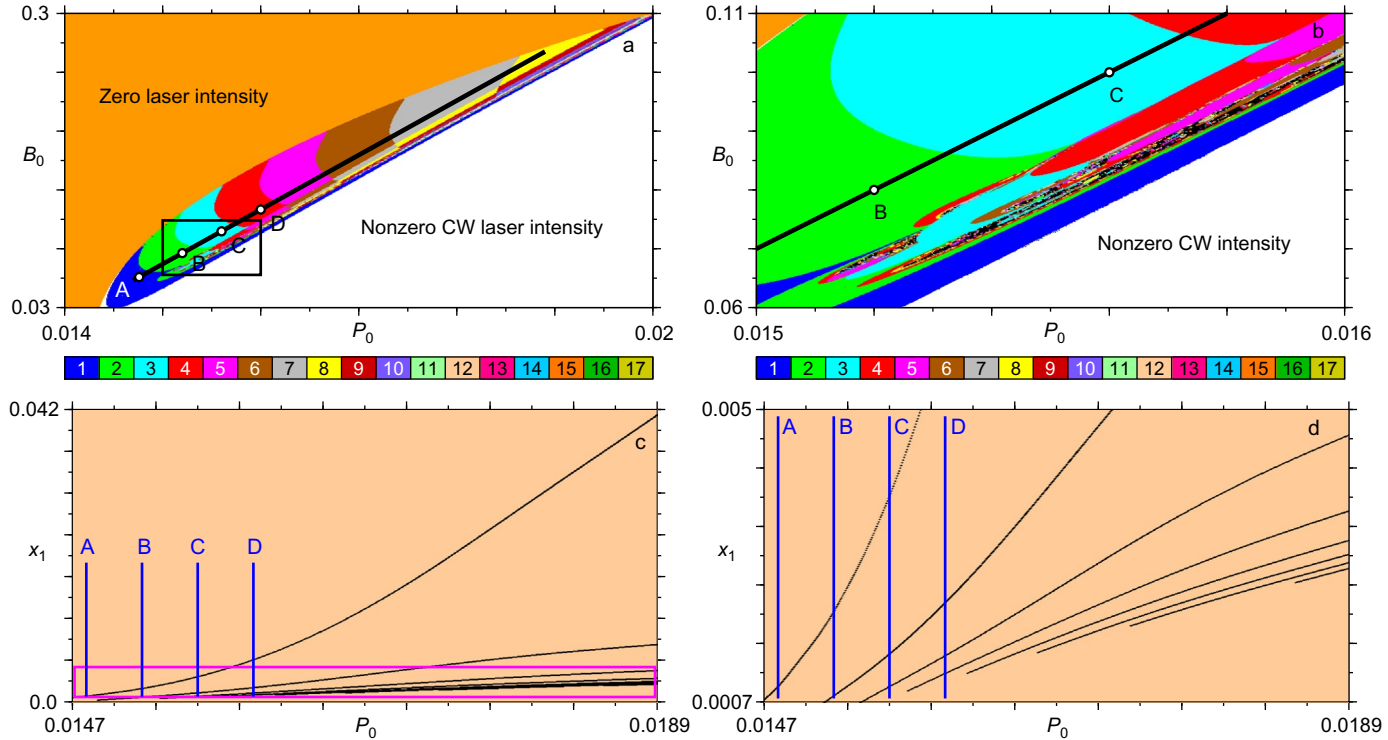


Fig. 14 (a) Nonchaos-mediated spike-adding sequences of mixed-mode oscillations recorded in the laser intensity oscillations as a function of the pump parameter P_0 and the bias voltage B_0 . This control plane is dominated by large domains of zero and nonzero continuous wave laser intensities. (b) Magnification of the *black rectangle* seen in (a). (c) Bifurcation diagram displaying local maxima of the laser intensity, x_1 , each one of such maxima resulting in one branch of the bifurcation diagram. The diagram illustrates the build-up of the spike-adding-sequence along the *black line* in (a) and (b) when P_0 and B_0 are increased simultaneously. Points A, B, C, and D are located at $(P_0, B_0) = (0.0148, 0.06)$, $(0.0152, 0.08)$, $(0.0156, 0.1)$, and $(0.016, 0.12)$, respectively. (d) Details of the spike-adding sequence inside the *violet (gray in the print version) box* at the bottom of the plot in (c). Source: Panel (a): From Freire, J.G., Meucci, R., Arcchi, F.T., Gallas, J.A.C., 2015. Self-organization of pulsing and bursting in a CO_2 laser with opto-electronic feedback. *Chaos* 25, 097607.

shows a global view of the control plane defined by the pump parameter P_0 and the bias voltage B_0 . As illustrated in Fig. 14a, this space is dominated by large domains of zero and nonzero CW laser intensities. Separating these two domains there is a stripe of parameters along which there is a plethora of laser oscillations organized in a regular way. Similarly to what happens in the plane $R \times B_0$ (Fig. 13), the plane $P_0 \times B_0$ also shows that the complexification of the laser intensity occurs via nonchaos-mediated spike-adding mixed-mode oscillations. This is corroborated clearly by the bifurcation diagrams in Fig. 14c and d. Such diagrams were drawn by tuning P_0 and B_0 simultaneously along a portion of the black auxiliary line in (a) and (b). The vertical lines in (c) and (d) indicate the position of the four representative points A, B, C, D marked in the stability diagrams (Fig. 14a and b).

Fig. 15 shows the distribution of laser phases recorded for the parameter space defined by the control of the unperturbed cavity losses k_0 vs the modulation strength k_1 . This plane contains a remarkable feature, namely the mosaic-like tiling that accumulates from right to left inside the vertical rectangle seen on the left side of Fig. 15a. Such tiling consists of an apparently infinite sequence of stability phases that arises from the regular way that spikes are added to the laser intensity pulse when both parameter are tuned. As may be seen from the figure, the mosaic consists of adjacent phases characterized by waveforms where the number of spikes grows horizontally from right to left as k_0 decreases, and grows from bottom to top, as k_1 increases. This type of change implies the existence of two types of parameter paths, one for “horizontal” nonchaos-mediated spike-adding sequences of mixed-mode oscillations, and another one, *transversal*, for “vertical” sequences. Note that observation of such mosaic requires tuning two parameters simultaneously, something not usually done in experiments. A similar mosaic-like tiling was observed in a rather distinct system, a driven chemical reaction known as the *Brusselator*, where the mosaic is found in the limit of small driving frequencies and in a region where chaos is virtually absent (Gallas, 2015).

The parameter region inside the rightmost rectangular box in Fig. 15a is shown magnified in Fig. 15b, and the pair of boxes in it are enlarged in Fig. 15c and d. Fig. 15c and d illustrates regions where chaos is quite abundant. Fig. 15c shows a typical configuration found in many places in control space: oscillatory lasers modes emerge organized in very complicated ways which are simply too complex to be described by other than graphical means. In contrast to the strong phase entanglement seen in Fig. 15c, Fig. 15d shows infinite sequences of phases displaying the same regular

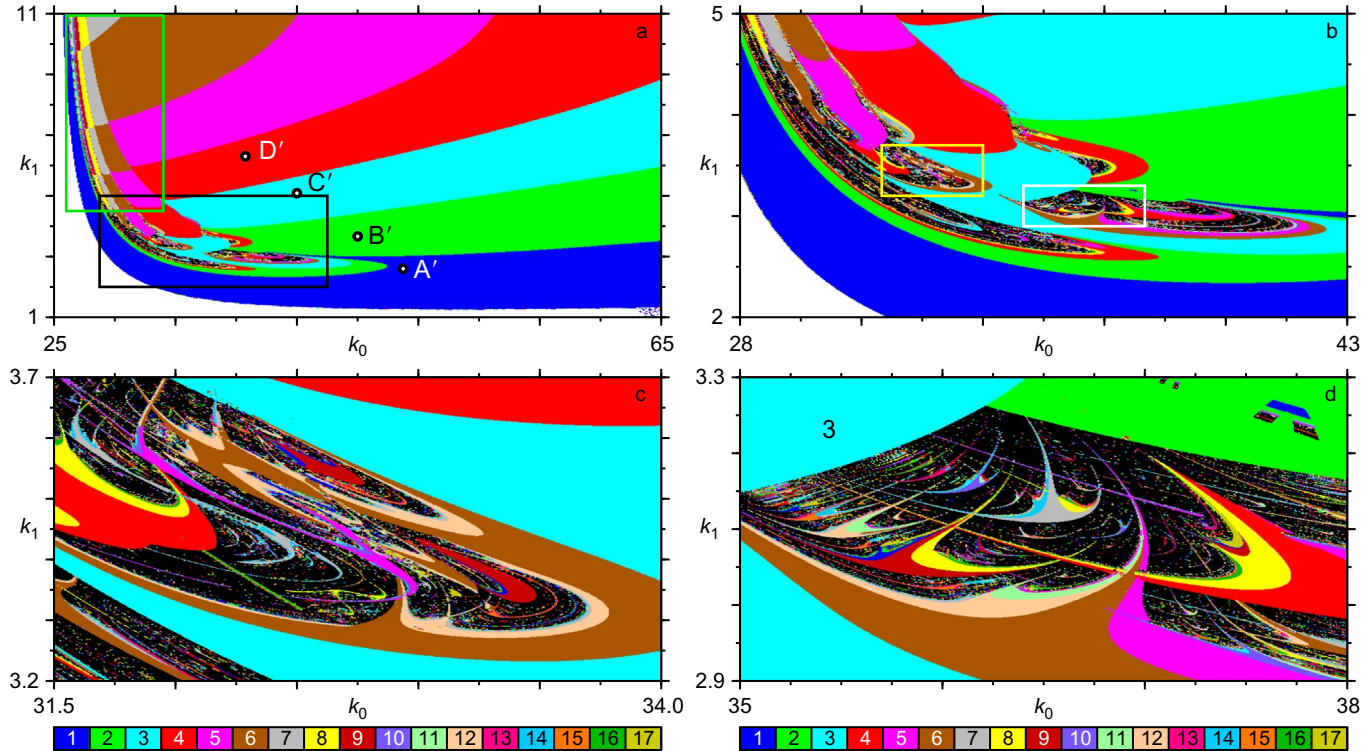


Fig. 15 (a) Nonchaos-mediated spike-adding sequences of mixed-mode oscillations recorded as a function of k_0 , the control of the unperturbed cavity losses, and k_1 , the modulation strength. This control plane is dominated by periodic laser spiking. The *mosaic-like* pattern inside the *vertical rectangle* is enlarged in Fig. 18. (b) Magnification of the *black horizontal rectangle* in (a). (c) Magnification of the *leftmost rectangle* in (b). (d) Magnification of the *rightmost rectangle* in (b). The *number 3* marks the domain toward which both 3-spikes adding cascades accumulate. Note the similarity of the shrimp accumulations in this panel with the ones in Fig. 12.

spike-adding systematics found previously in the upper panels in Fig. 12, accumulating toward a large 3-spikes phase.

How similar are the mixed-mode oscillations observed in the CO₂ laser with feedback when parameters are tuned? The answer is given in Fig. 16 which illustrates the great similarity of mixed-mode oscillations typically observed when tuning rather distinct control parameters of the laser. In the top row of Fig. 16 we plot the first four of an apparently infinite sequence of consecutive spike additions observed in the $P_0 \times B_0$ control plane. These four panels correspond to the points labeled A, B, C, D in Fig. 14a, with coordinates $(P_0, B_0) = (0.0148, 0.06), (0.0152, 0.08), (0.0156, 0.1), (0.016, 0.12)$, respectively. For comparison, the bottom row shows an analogous sequence, but observed while tuning parameters in the $k_0 \times k_1$ plane for points A', B', C', D' in Fig. 15a, with coordinates $(k_0, k_1) = (48, 2.6), (45, 3.666), (41, 5.088), (37.3, 6.404)$, respectively. Noteworthy is the fact that, although the periods of both sequences of spikes are initially very different, after just four spike additions they already are of the same order of magnitude, suggesting that the growth of the period may not be unbounded.

Fig. 17a shows a global description of the spike unfolding recorded on the $R \times P_0$ control plane. This plane also shows regular laser pulsations organized according similar spike-adding scenarios as previously found in other control planes. In contrast with previous situations, in this parameter plane it is quite easy to follow spike-adding sequences by tuning just a single parameter, R , instead of a pair of parameters, as before. Furthermore, as illustrated in Fig. 17b and c, it is not any path across the control space that will reveal its regular organization and mixed-mode oscillations. For instance, as depicted in panels Fig. 17d–f, bifurcations along vertical one-parameter lines will typically result in rather unusual series of spikes, mediated or not by chaos. To uncover the mechanism responsible for such complex and apparently nonsystematic spike unfoldings remains an open challenge.

The temporal evolutions in Fig. 17d–f show a close resemblance to those in Fig. 16, despite the fact that they are obtained by sweeping rather distinct parameters. The high number of parameters involved and the great variety of spikes arrangements that were observed prevent one from attempting a general classification. But such classification is obviously an important and enticing problem that needs to be eventually addressed.

We now investigate what happens with the laser intensity in Fig. 18a, a magnification of the leftmost (vertical) rectangle in Fig. 15a. As already mentioned, this region contains large stability phases forming a mosaic-like tiling that accumulates in Fig. 18a from right to left and from bottom to top.

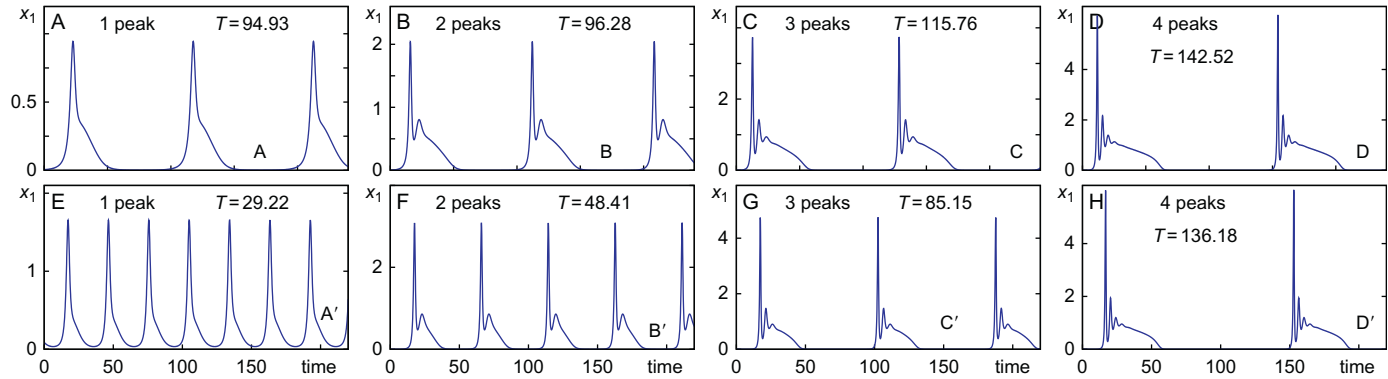


Fig. 16 Two similar looking sequences of spike-adding mixed-mode oscillations for x_1 as a function of time, recorded while tuning rather distinct laser control parameters. Top row: temporal evolutions for points labeled A, B, C, D on the $P_0 \times B_0$ plane of Fig. 14a. Bottom row: temporal evolutions for points A', B', C', D' on the $k_0 \times k_1$ plane of Fig. 15a. Time and period T of the oscillations are in arbitrary units. For convenience, the vertical axis shows $x_1 \times 10^3$.

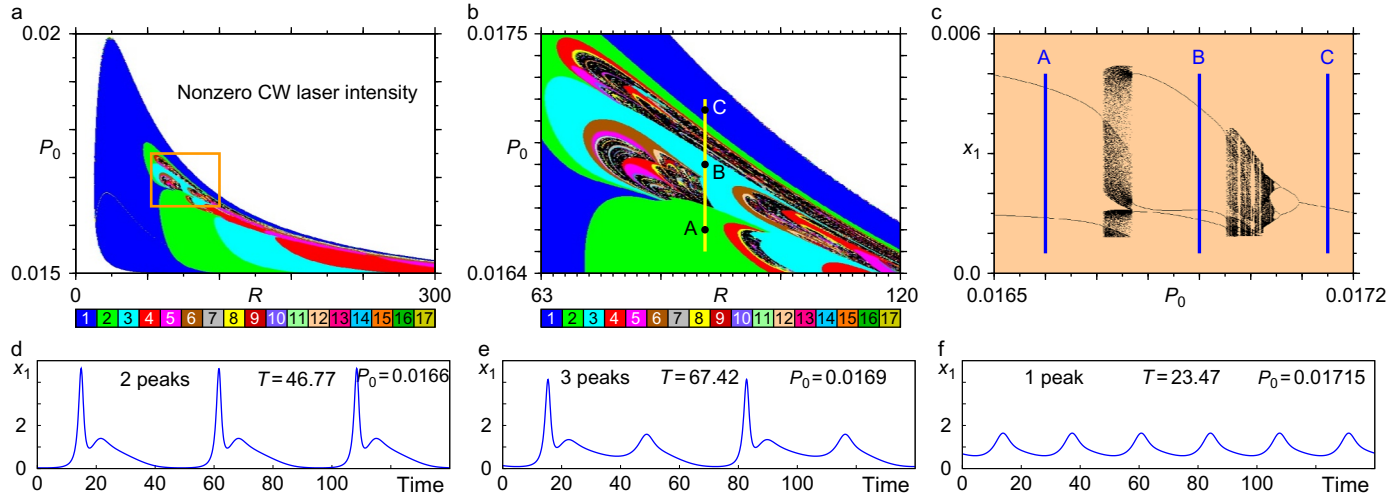


Fig. 17 (a) Global view of the spikes distribution in the $R \times P_0$ plane illustrating spike-adding cascades and predominance of CW laser modes. (b) Magnification of the box in (a) showing (in black) the presence of chaotic laser bursting. (c) Bifurcation diagram displaying intensity maxima obtained for $R = 89$, along the vertical line in (b). (d–f) Laser intensity x_1 vs time (in arbitrary units) for A, B, C as indicated in (b) and (c). T denotes the period of the oscillation in arbitrary units. For convenience, the vertical axis shows $x_1 \times 10^3$.

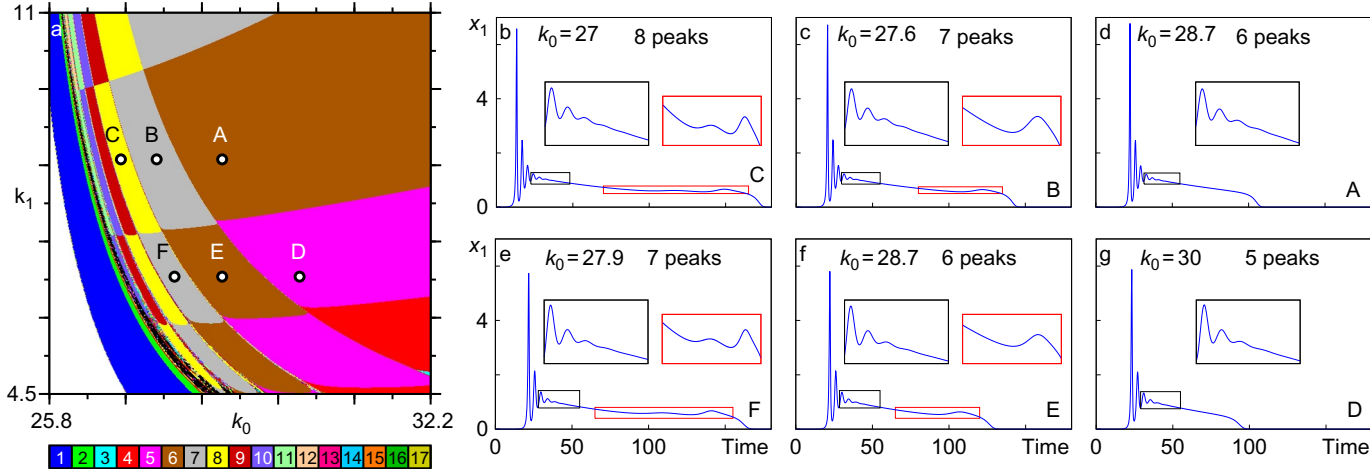


Fig. 18 (a) Enlargement of the *vertical rectangle* in Fig. 15a illustrating the mosaic-like pattern and remarkable systematic shifts of the laser pulsations. (b–g) Temporal evolutions of the laser pulses $x_1(t)$ showing the genesis of new spikes (through waveform deformations (Junges and Gallas, 2012a,b)) underlying the mosaic-like pattern. The respective periods of oscillation are $T_A = 300.58$, $T_B = 342.09$, $T_C = 377.97$, $T_D = 172.47$, $T_E = 210.46$, and $T_F = 245.92$, in arbitrary units. Such tiling repeats over an extended region of the control space. For convenience, the *vertical axis* shows $x_1 \times 10^3$.

We consider the waveforms along two representative stripes of such tiling: for the points A, B, C along the line $k_1 = 8.5$, and for points D, E, F along $k_1 = 6.5$.

As evidenced by Fig. 18b–g, the complexification of the waveforms underlying the mosaic-like tiling involves two concurrent mechanisms which act on the large plateau contained in the periodic oscillations: when parameters are tuned, the plateau develops more and more undulations on both extremities. On the left-hand side of the plateau one finds a complexification that unfolds in a similar way as already described in Fig. 16 for the mixed-mode oscillations. The novelty here is that, simultaneously, there is a complexification at the right-hand-side extremity of the plateau, also by the addition of spikes. Thus, the mosaic-like tiling accumulation seems to originate from a *double winding of the trajectories* in phase space. While double windings have certainly been described abundantly in connection with homoclinic orbits and with other sophisticated forms of unstable mathematical phenomena, we are not aware of the impact of any of these phenomena being described in parameter space. In contrast with homoclinic phenomena, the double winding mentioned here (i) is manifestly connected with *stable* trajectories and (ii) is clearly responsible for inducing regularities in large portions of the control parameter space. Recall that, while there is a profusion of studies dealing with the intricacies of complex phenomena in phase space, most of them refer to systems whose laboratory implementation is difficult. Our diagrams, however, display the global organization of stability phases and, therefore, are directly measurable with present-day technology. For instance, a recent comparison between measurements and predictions for an electronic device found them to be in rather good agreement over wide two-dimensional control parameter windows (Sack et al., 2013).

Is the mosaic-like tiling a particularity of the $k_0 \times k_1$ control plane (Fig. 18), or is it a generic feature? To check this, we computed high-resolution phase diagrams for the control plane defined by the bandwidth α and amplification β of the laser, shown in Fig. 19. As it is evident from Fig. 19a, this control plane displays also a mosaic-like tiling. As before, this plane shows a large predominance of periodic over chaotic laser modes.

On the bottom of Fig. 19a one sees a thin rectangular box, shown magnified in Fig. 19b. From this magnification one sees that chaos (represented in black) arises from certain “wrinkles” that develop in the phases of regularity that, for larger values of β , combine to form the mosaic-like tiling. Although chaotic phases are quite small compared to the overwhelmingly

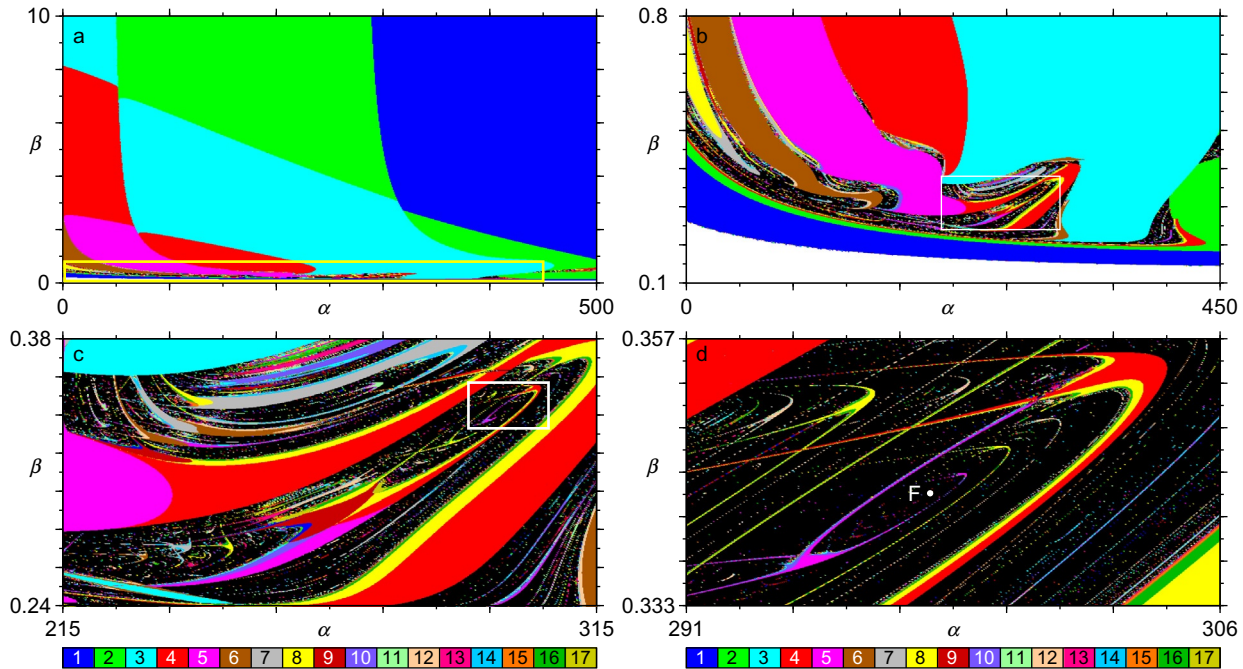


Fig. 19 (a) Mosaic-like pattern in the bandwidth α vs amplification β control plane. (b) Magnification of the box in (a) illustrating the presence of "wrinkles" (see text). (c) Magnification of the box in (b). (d) Magnification of the box in (c) illustrating an infinite hierarchy of nested spirals of chaos and of regularity converging to the focal hub F near $(\alpha, \beta) = (297.85, 0.3431)$.

large regular phases, they can be probed experimentally without problem with modern technology. In fact, as discussed in [Section 3.3.1](#), chaos in CO₂ lasers with feedback was already reported in many experiments. What is still open is a systematic experimental scan of the control parameter space, similar to what was done here numerically. Experimental scans can corroborate or uncover shortcomings of the model used in the numerical analysis.

The chaotic phases of the CO₂ laser with feedback are full of rich dynamics, also waiting for a systematic exploration. For instance, [Fig. 19c](#) shows a magnification of the box in [Fig. 19b](#). This figure illustrates once again the complex alternation of chaotic and regular stability phases of the lasers, similar to the situation described earlier for [Fig. 15c](#). However, chaotic phases also harbor wide regions of regularity, as exemplified by [Fig. 19d](#), an enlargement of the rectangle in [Fig. 19c](#). [Fig. 19d](#) illustrates an infinite sequence of spirals of chaos and spirals of regularity that arise around certain exceptional points in control space, called *periodicity hubs*, well known to organize the dynamics over extended parameter regions ([Barrio et al., 2011](#); [Bonatto and Gallas, 2008b](#); [Freire and Gallas, 2010](#); [Gallas, 2010](#); [Gallas et al., 2014](#); [Vitolo et al., 2011](#)). The exceptional point responsible for the large anticlockwise spiraling in [Fig. 19d](#) is located at the periodicity hub F , numerically estimated to be near $F = (\alpha, \beta) = (297.85, 0.3431)$. An infinite quantity of similar hubs is known to exist in the vicinity of F , as elaborated in [Gallas \(2010\)](#) and [Vitolo et al. \(2011\)](#). Summarizing, intricate alternations of chaos and regularity can be observed abundantly in every section of the control space.

3.3.3 Arborescent Structures Generated by Spikes Transitions

Several diagrams above, like, eg, [Figs. 17](#) and [18](#), have shown that the number of spikes evolves continuously, changing smoothly, and regularly in well-localized regions of the control space. When moving along shrimp legs one finds that they contain an infinite number of transition boundaries where the number of spike changes and it is natural to ask how such transitions occur. Two examples of such transitions are shown in [Fig. 20a](#) and [b](#), where the numbers refer to the number of spikes characterizing the region containing them. One sees that spike-adding occurs longitudinally, ie, along shrimp legs, while spike doubling occurs predominantly in the transverse direction.

This surprising and unexpected regularity underlying waveform complexification by spike adding and doubling is summarized schematically in [Fig. 20c](#). In this figure, the two outermost horizontal stripes denote regions confining a shrimp leg. The boundaries b_0 and b_1 on the top define the

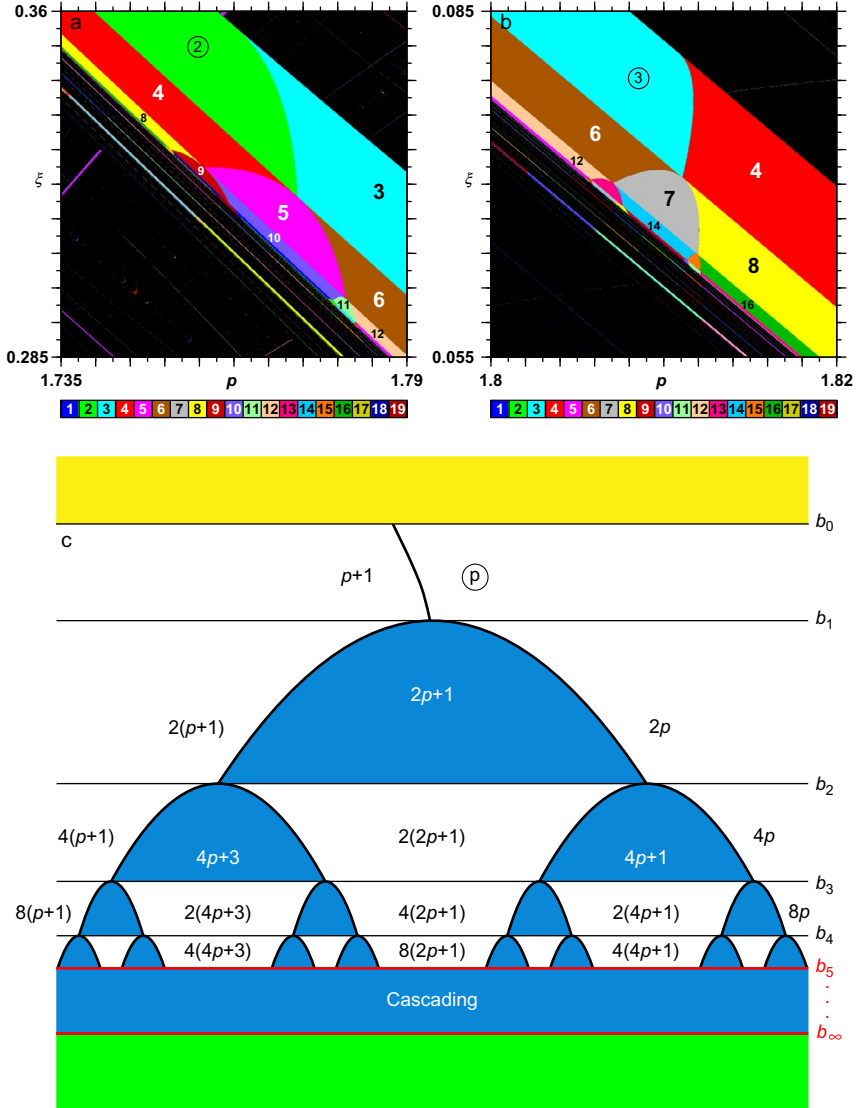


Fig. 20 The generic arborescent structures generated by spikes transitions when moving along thin segments formed by periodic phases like the ones in Fig. 19c and d. (a) Leftmost panel on the top: Arborescent structure generated by a $2 \rightarrow 3$ transition. (b) Rightmost panel on the top: Arborescent structure generated by a $3 \rightarrow 4$ transition. Both cases are discussed in detail by Gallas et al. (2014). (c) Bottom panel: Schematic representation of the combined spike adding and doubling mechanisms involved in (a) and (b). Blue (gray in the print version) regions always contain odd periods. In the top stripe, the location of the blue (gray in the print version) region depends if p is odd or even.

horizontal stripe $s_0 \equiv b_1 - b_0$ along which some *main* spike number p changes to $p + 1$ along a smooth boundary. In each subsequent stripe $s_k \equiv b_{k+1} - b_k$, for $k = 1, 2, 3, \dots, \infty$, the number of spikes grows from $2^k p$ to $2^k(p + 1)$ by acquiring additional spikes through smooth wave-pattern deformations similar to the ones observed in infinite-dimensional systems involving delayed feedback (Junges and Gallas, 2012a,b; Junges et al., 2013). The spike unfolding illustrated in Fig. 7 is organized in a characteristic tree resembling a bifurcation diagram. This *arborescent* organization may be observed profusely in other regions of the control space, independent of the variable used to count the spikes. This same organization was also observed in other familiar flows like, eg, in a tritrophic food chain model, in the Hindmarsh–Rose model, in a model of neocortical neurons, in a model of a vertical-cavity surface-emitting laser (VCSEL), in a semiconductor laser with injection, in Rössler’s oscillator, and in the self-pulsations of a CO₂ laser with feedback (see, for instance, figure 1b in Junges and Gallas, 2012a). Therefore, the arborescent trees in Fig. 20 should be a robust property of flows, a signature of a systematic wave-pattern complexification mechanism acting through a simultaneous spike adding and doubling continuous deformations of periodic oscillations in dissipative nonlinear systems. The mathematical mechanism generating these arborescent trees is not known yet.

3.4 Delayed Feedback, Infinite Dimension

3.4.1 The General Model

Section 3.2 considered the three-dimensional model of the CO₂ laser under the assumption that the feedback occurred instantaneously. A natural question to ask is what happens for the more realistic situation when the feedback occurs after some finite delay τ of arbitrary duration. In the literature one finds studies for very large or small delays. However, the impact of delays with arbitrary duration is not yet known. The aim of this section is to consider feedback delays of arbitrary duration, following Junges and Gallas (2016).

Delayed feedback is simulated using the same standard model defined in Eqs. (5)–(7) (Arecchi et al., 1991; Junges and Gallas, 2012a) but including now the delay τ :

$$\dot{x} = kx(\gamma - 1 - \alpha \sin^2(z(t - \tau))), \quad (21)$$

$$\dot{y} = \gamma(A - y - xy), \quad (22)$$

$$\dot{z} = \beta(B - rx - z). \quad (23)$$

As before, k stands for unmodulated cavity losses, γ for the population decay rate, β for the damping rate of the feedback loop, r is the feedback

gain, B is the bias voltage applied to an electro-optic modulator, A is the normalized pump parameter, and α is the amplitude of the modulation (Wang et al., 1990). As usual (Arecchi et al., 1986; Junges and Gallas, 2012a; Wang et al., 1990), B is normalized to $1/\pi$ times the half wavelength voltage of the modulator. Following the literature, we fix $A = 1.66$, $\alpha = 5.8$, $k = 9.6 \times 10^6 \text{ s}^{-1}$, $\gamma = 0.03 \times 10^6 \text{ s}^{-1}$, $\beta = 0.5 \times 10^6 \text{ s}^{-1}$. The main goal is to describe how the stability domains in the $r \times B$ control plane change when tuning τ . The stability diagrams obtained Section 3.2 for $\tau = 0$ serve as reference against which to compare the changes induced by the delay.

Eqs. (21)–(23) are also numerically integrated with the standard fixed-step fourth-order Runge–Kutta algorithm, over a mesh of equally spaced points. For each pair of parameters, integrations started always from the same initial conditions $x(0) = y(0) = 1$ and the same initial history $z(-\tau, 0) = 1$.

Figure 21 displays a series of snapshots for the values of τ indicated. From this figure, one can recognize the sizable changes undergone by the stability islands when the delay increases from $\tau = 0$ up to $\tau = 30$, in units of 10^{-6} s . For $\tau = 0$ (no delay), the top leftmost panel in Fig. 21 coincides with Fig. 7a, as expected. The remaining panels illustrate what happens as τ grows. Recall that for $\tau \neq 0$ the dimensionality (number of degrees of freedom) of the laser equations jumps abruptly and discontinuously from three to infinity.

As the delay increases, the region of complex periodic and nonperiodic oscillatory solutions displaying more than one peak per period shrinks fast, until $\tau \approx 0.5 \mu\text{s}$, when only a large domain of 1-spike pulsations survives. This large 1-spike region persists up to about $\tau \approx 1.5 \mu\text{s}$, when a green (light gray in the print version) region associated to solutions with two spikes per period returns. Further increase of the delay time makes this two-peak region to grow steadily. Additionally, some complicated arrangements of “islands” of solutions with different number of peaks start to develop. Some of these islands lie inside the boxes contained in the stability diagrams from $\tau = 2.7 \mu\text{s}$ to $\tau = 4 \mu\text{s}$. As these islands grow, additional islands proliferate inside of them, revealing nested series of peak-doubling and peak-adding cascades that lead to a region of chaotic oscillations inside these concentric islands. By further increasing the delay ($\tau > 4 \mu\text{s}$), the region of chaotic solutions grows and develops accumulations of shrimps inside them. At this stage, the dynamics is very complex and rich as shown in the diagrams with delay time $\tau > 5 \mu\text{s}$. The narrow white horizontal stripes on the top of the diagrams in Fig. 21 represent parameter values for which the laser output is identically zero. Below such white stripes, the narrow black phases represent solutions with a period too big to be ascertained without much

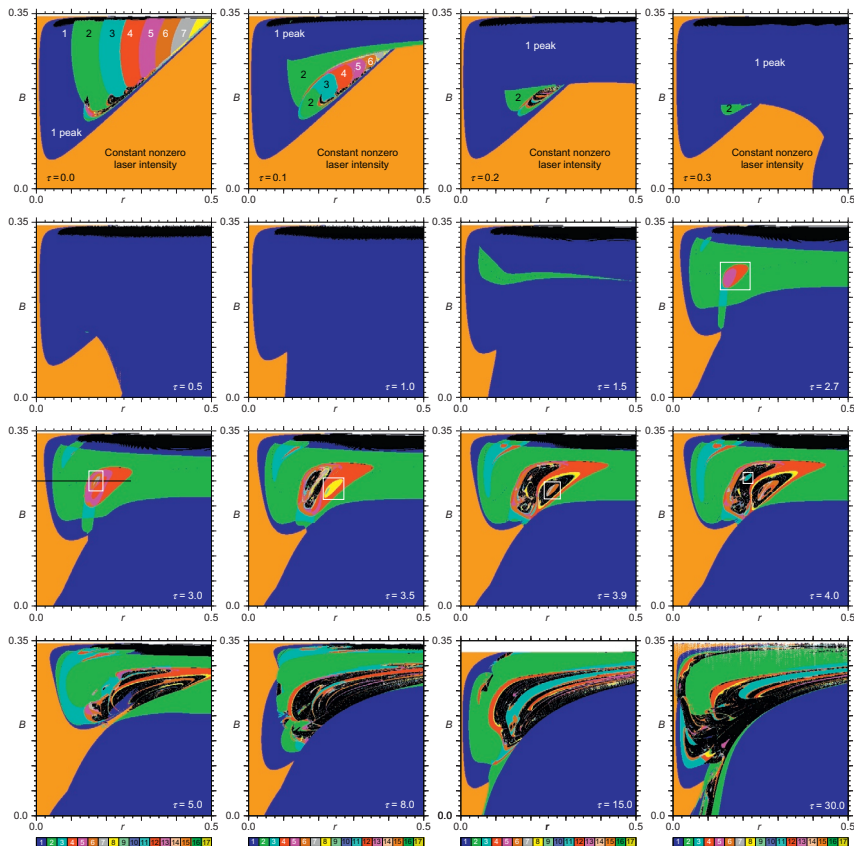


Fig. 21 Evolution of the laser stability diagram when the delay τ (in μs) increases. For $\tau = 0 \mu\text{s}$ there is a horizontal spike-adding cascading of pulses: pulses in adjacent windows differ by one spike. Between $\tau = 0.1 \mu\text{s}$ and $\tau = 1 \mu\text{s}$ the region containing such windows is strongly reduced, with one-peak oscillations dominating. Then, complex phases emerge again, with rather intricate distributions of pulses as τ grows. The panel for $\tau = 3 \mu\text{s}$ shows a horizontal line for $0 < r < 0.27$ at $B = 0.25$. A bifurcation diagram along this line is discussed in Fig. 22. Each panel depicts full phase-space analysis performed for $400 \times 400 = 1.6 \times 10^5$ parameter points.

numerical effort. For a detailed description of the divergence of the period in this region, see Junges and Gallas (2012a) and Yang et al. (1997).

An important point to note is the relative *invariance* of the large 1-spike phase observed for $0.5 \lesssim \tau \lesssim 1.0 \mu\text{s}$ that separates two regimes where rich dynamical activity is observed when tuning τ . The differences in the qualitative behavior observed before and after this rather bulky invariant interval of τ emphasize the importance of the numerical calculation presented here.

Most analytical work done in the context of delay-differential equations is valid only as small-delay approximations (Erneux and Glorieux, 2010). The intricate dynamical organization of stability phases described here is well beyond reach of analytical approximations.

The complexities associated with nonzero delay times were described recently in a video (Junges and Gallas, 2016) showing the evolution of the $r \times B$ stability chart like in Fig. 21, but varying the delay more finely, namely for 200 equally spaced snapshots covering the interval $\tau \in [0, 10] \mu\text{s}$. Such video provides an animation of what happens when the delay is varied continuously. For instance, it allows one to identify more precisely the three regimes discussed earlier, in connection with Fig. 21. Initially, for $\tau \in [0, 0.55] \mu\text{s}$, parameter phases depicting oscillations having more than one peak per period shrink in size until they disappear completely. Then, for $\tau \in [0.55, 1.1] \mu\text{s}$ only a big phase corresponding to one-peak modes is present. Along both intervals, $[0, 0.55]$ and $[0.55, 1.1]$, the lower part of the stability charts, initially orange (representing constant nonzero laser amplitudes), becomes more and more dominated by one-peak laser modes. The sequential emergence of islands related to more complex periodic and chaotic oscillations (described in Fig. 21) becomes clearly discernible. The video provides a clear view of the complicated drift of stability domains in the $r \times B$ diagram, specially about the speed of changes, showing how the domains reshape themselves and collide to form new complicated structures. For instance, the contraction rate of complex periodic and chaotic phases over the range $\tau \in [0, 0.55] \mu\text{s}$ seems to be greater than the growth rate of such complex phases after the “invariance” period ($\tau > 1.1 \mu\text{s}$). This suggests that to operate the laser on a given specific complex oscillation can be experimentally more challenging at relatively small delays, due to the greater sensibility of the stability domains to the delay. Despite the high computational cost, the video provides unique and useful informations about the laser, informations that are virtually impossible to obtain by other means.

3.4.2 Bifurcations by Waveform Deformation

As described earlier, an increase of τ tends to change the diagrams of Fig. 21 in a such way that islands of periodic solutions emerge embedded inside wide regions associated to solutions with a specific number of peaks, or inside regions of nonperiodic (chaotic) behavior. The dynamical features observed inside these islands get more complex as τ evolves. To clarify how the laser output generates such structures, the bifurcation diagram shown on the top row of Fig. 22 was computed along the black horizontal line in the panel for

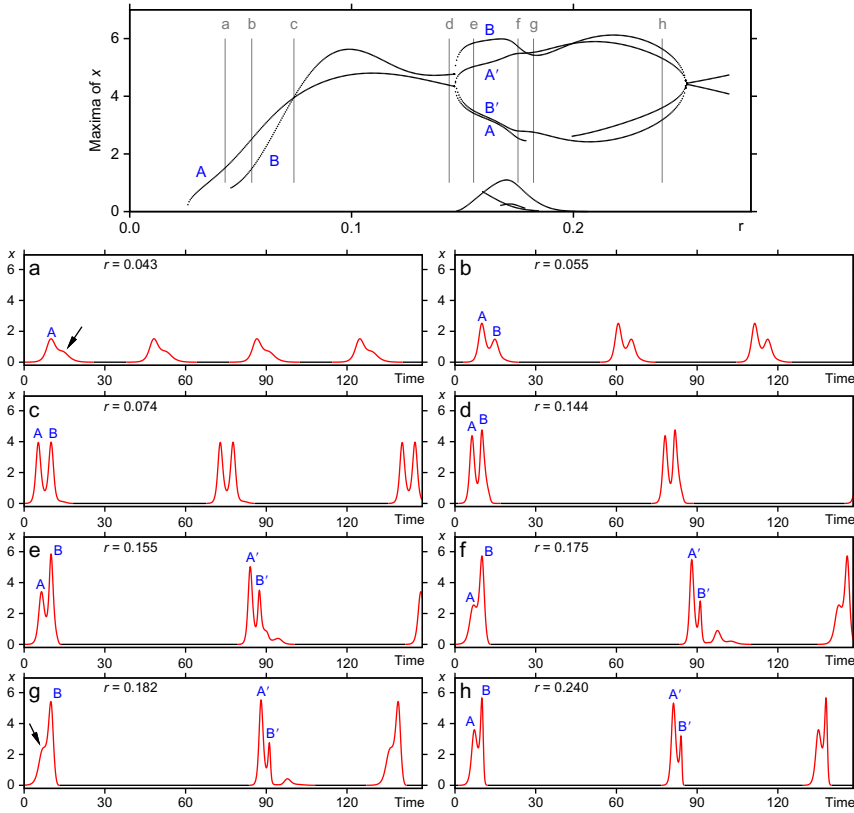


Fig. 22 Top panel: bifurcation diagram for $0 < r < 0.27$, $B = 0.25$, and $\tau = 3 \mu\text{s}$ (as indicated by the *black line* in the corresponding panel in Fig. 21). Below the bifurcation diagram, panels (a–h) display the temporal evolution $x(t)$ for values of r indicated by the *vertical lines* in the bifurcation diagram. *Black horizontal segments* on the bottom indicate laser off (ie, $x < 0.005$).

$\tau = 3.0 \mu\text{s}$ in Fig. 21, for parameters values along the concentric islands located inside the green (light gray in the print version) region (2 peaks). Such diagram displays a clear peak-doubling bifurcations combined with the abrupt appearance and disappearance of isolated branches, resulting from peak-generation by continuous deformation of the laser signal as the parameter is varied (the “peak-adding phenomenon” (Junges and Gallas, 2012a,b)). Fig. 22a–h shows the temporal evolution of the laser intensity x (in arbitrary units) for selected values of r , indicated by vertical lines in the bifurcation diagram. Fig. 22a shows peak A corresponding to branch A of the bifurcation diagram. The arrow in Fig. 22b indicates a deformation in the laser pulse that, upon further increase of r , gives origin to a new peak B, associated with branch B. Initially, the amplitude of peak B is smaller than

A, but as r increases, its amplitude grows fast so that, eventually, B becomes larger than A. This unfolding can be followed in Fig. 22b–d. As r further increases past a bifurcation which occurs for $r \approx 0.146$, peaks A and B split into doublets (A,A') and (B,B'), as shown in Fig. 22e. This happens such that peak A', born smaller than B, grows faster than B, overtaking it at $r = 0.179$ and remaining so until $r = 0.199$, when peak B becomes bigger again. The curious fact observed here is that in the range of r where A' remains bigger than B, the peak A disappears, turning to appear just when B becomes bigger than A' again. This phenomenon is clearly seen in Fig. 22f–h and following the evolution of the branches B, A', and A in the bifurcation diagram. Note that peak A disappears smaller and reappears larger than B'.

In addition to the remarkable large-peak dynamics described earlier, Fig. 22 also contains a series of nonlabeled small peaks, visible at the bottom of the bifurcation diagram and immediately after the peak B' in Fig. 22e–g. The unfolding of these smaller peaks is shown magnified in Fig. 23. The branches resulting from these small peaks are located inside the green (gray in the print version) box on the bifurcation diagram in the leftmost panel on the top row of Fig. 23. The rightmost panel shows a magnification of the green (gray in the print version) box. Initially (low values of r), Fig. 23a shows peak C and the deformation (indicated by the arrow) that gives birth to peak D seen in Fig. 23b. Similarly, Fig. 23b shows peaks C and D and the new deformation responsible for the birth of peak E in Fig. 23c. Fig. 23c and d shows three peaks C, D, and E whose amplitudes start to decrease when r further increases. Eventually, peaks E and D disappear as illustrated in Fig. 23e and f, respectively. This sequence indicates that the peak-adding mechanism also operates on a smaller scale in the system.

To complement the information extracted from the temporal evolution of the laser intensity x , we apply the tools used in Junges and Gallas (2012a) to analyze how the system behaves in the $\gamma \times z_\tau$ plane, where $z_\tau \equiv z(t - \tau)$. Distinctly from what was done in that papers, instead of z the variable z_τ is considered here because, as seen in Eq. (21), the time derivative of the intensity depends of the delayed value of the feedback voltage, ie,

$$\frac{dx}{dt} = kx(f(\gamma, z_\tau)) = kx(\gamma - 1 - \alpha \sin^2(z_\tau)). \quad (24)$$

Fig. 24 shows two curves on the $\gamma \times z_t$ plane: the first one, represented as a light parabolic arc, marks the solution of $f(\gamma, z_\tau) = 0$ (nullcline). The other curve records the locus (γ, z_τ) obtained by integration of Eqs. (21)–(23), where the black segments represent solutions with $x = 0$ and the red

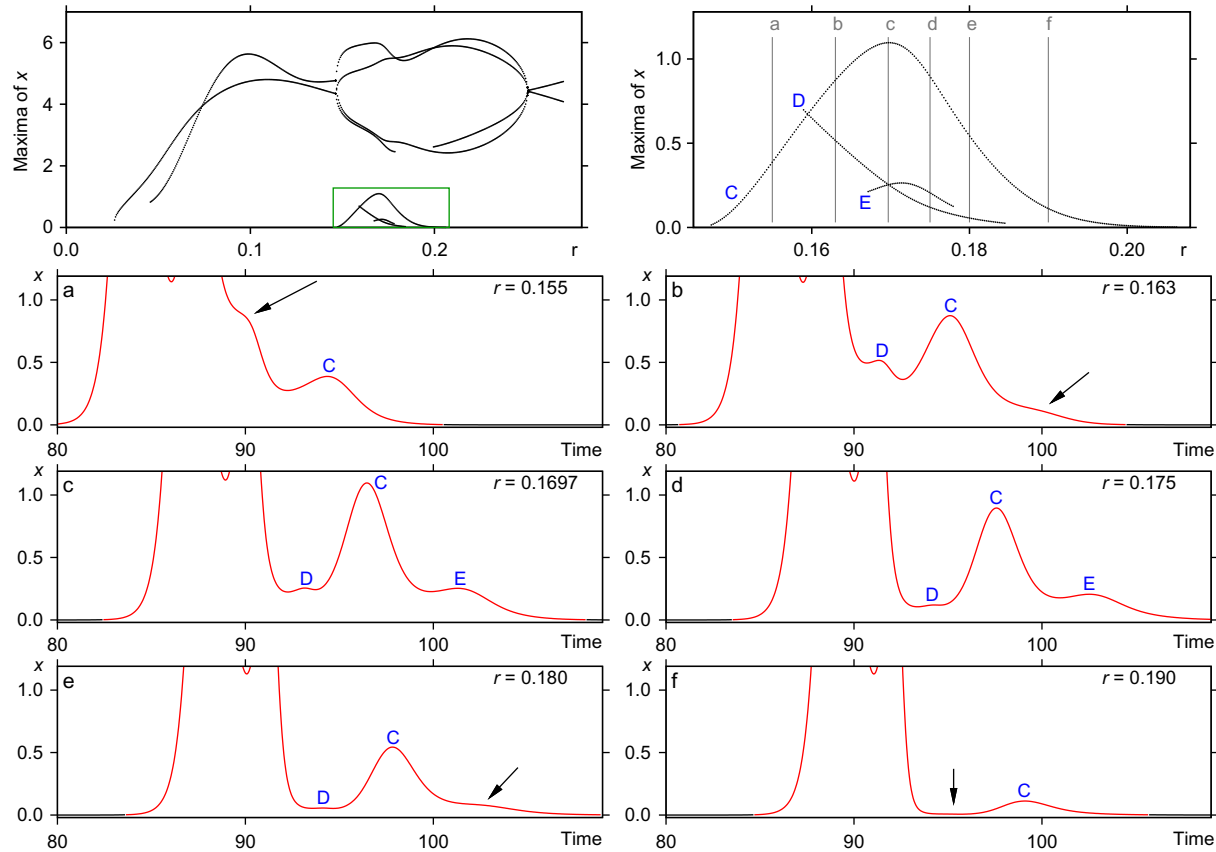


Fig. 23 Top left: bifurcation diagram of Fig. 22 with a box emphasizing low-amplitude oscillations. Top right: magnification of the box seen in the left panel, containing the low-amplitude oscillations. (a–f) Snapshots of the temporal evolution of $x(t)$, for values of r indicated by the vertical lines in the magnification of the bifurcation diagram, evidencing the peaks associated with the small-scale dynamics.

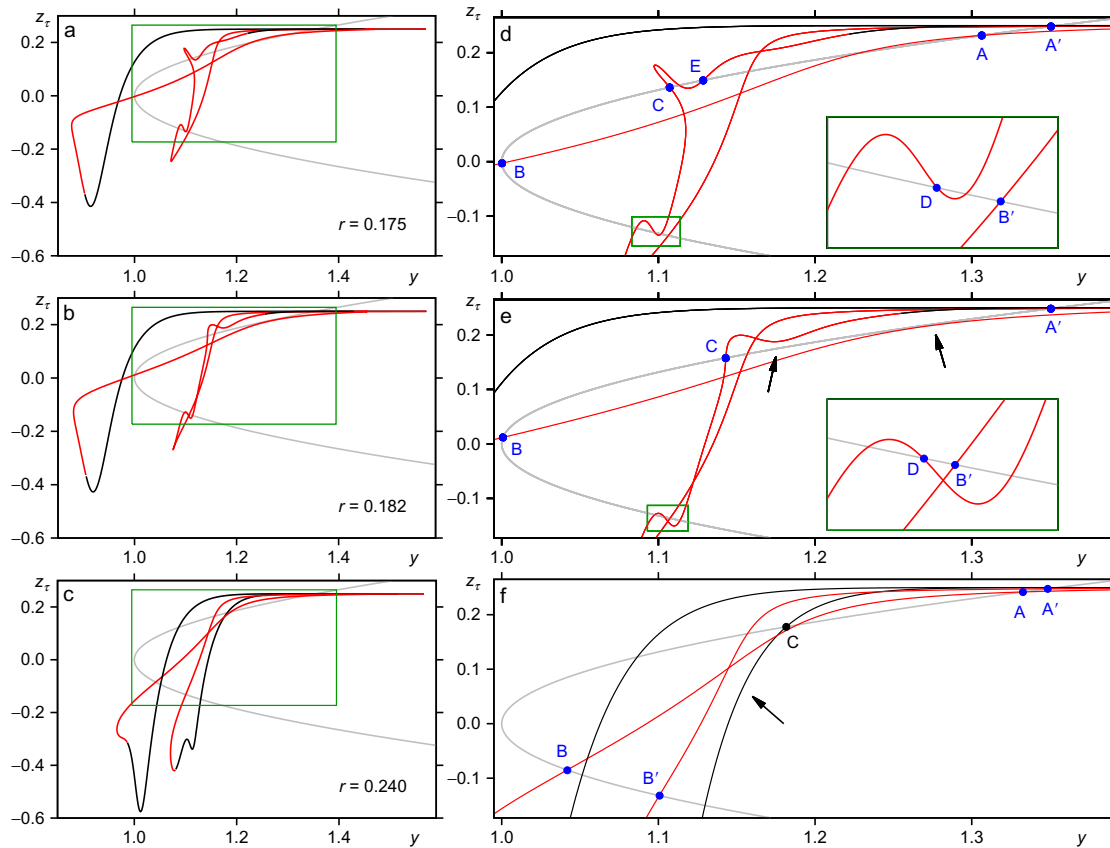


Fig. 24 (a–c) As before, trajectories in red (gray in the print version)/black indicate the locus (y, z_τ) , where $z_\tau = z(t - \tau)$, obtained by integration of Eqs. (21)–(23), and the gray arc indicates $f(y, z_\tau) = 0$. Intersections indicate extrema of x (see text). (d–f) Magnifications of the boxes of (a–c). Intersections associated with local maxima are indicated and labeled in blue (dark gray in the print version).

(gray in the print version) segments represent $x \neq 0$. The characteristic signature of the birth of a new isolated branch in the bifurcation diagram is the occurrence of *intersection points* between the nullcline and the red (gray in the print version) part of the locus.

Fig. 24a–c shows the complicated phase-space trajectories associated with the temporal evolutions presented in Fig. 22f–h. The green (gray in the print version) boxes inside them are magnified in Fig. 24d–f, respectively. In Fig. 24d, all the intersections related to local maxima are indicated by blue (dark gray in the print version) dots and labeled according to the associated peak. Nonlabeled intersections are related to local minima. When the bifurcation parameter is increased to $r = 0.182$, Fig. 24e shows that the trajectory is modified such that the intersections associated with peaks A and E disappear. The regions where these intersections disappear are indicated by black arrows. A further increase in r brings back the intersection associated with A, as shown in Fig. 24f, and a different type of behavior observed in phase space makes peak C to disappear. In the analysis of phase-space trajectories shown in Junges and Gallas (2012a,b), the death of a peak was associated with the deformation of the trajectory, in a way that the intersection of this trajectory with the nullcline no longer exists. However, from Eq. (24), one sees that there is another possibility to “undo” a peak: the solution may deform such that x becomes null in that segment. This can be recognized as follows. In Fig. 24e, the segment of the locus that intersects the nullcline at C is red (gray in the print version) (ie, $x \neq 0$) and, accordingly, point C corresponds to a peak in the temporal evolution. On the other hand, although in Fig. 24f the intersection between the nullcline and the locus still exists at C, it is no longer relevant because $x = 0$ in that segment of the locus (the segment is black, as indicated by the arrow). This means that peak C is no longer present in the temporal evolution, which is null. In other words, although the intersection associated with peak C is still present in the $\gamma \times z_\tau$ plane, the laser intensity vanishes in that segment.

3.4.3 Regularities in the $\tau \times r$ and $\tau \times B$ Control Planes

Next, the above analysis is extended by considering the modal structure of the laser in two additional control planes: $\tau \times r$ and $\tau \times B$. The main motivation is to learn what sort of changes modes undergo as a function of the feedback gain r and the bias voltage B applied to the electro-optic modulator when the delay τ is increased.

Fig. 25a represents stability domains (laser phases) over an extended portion of the $\tau \times r$ plane, computed for $B = 0.25$, the same value used

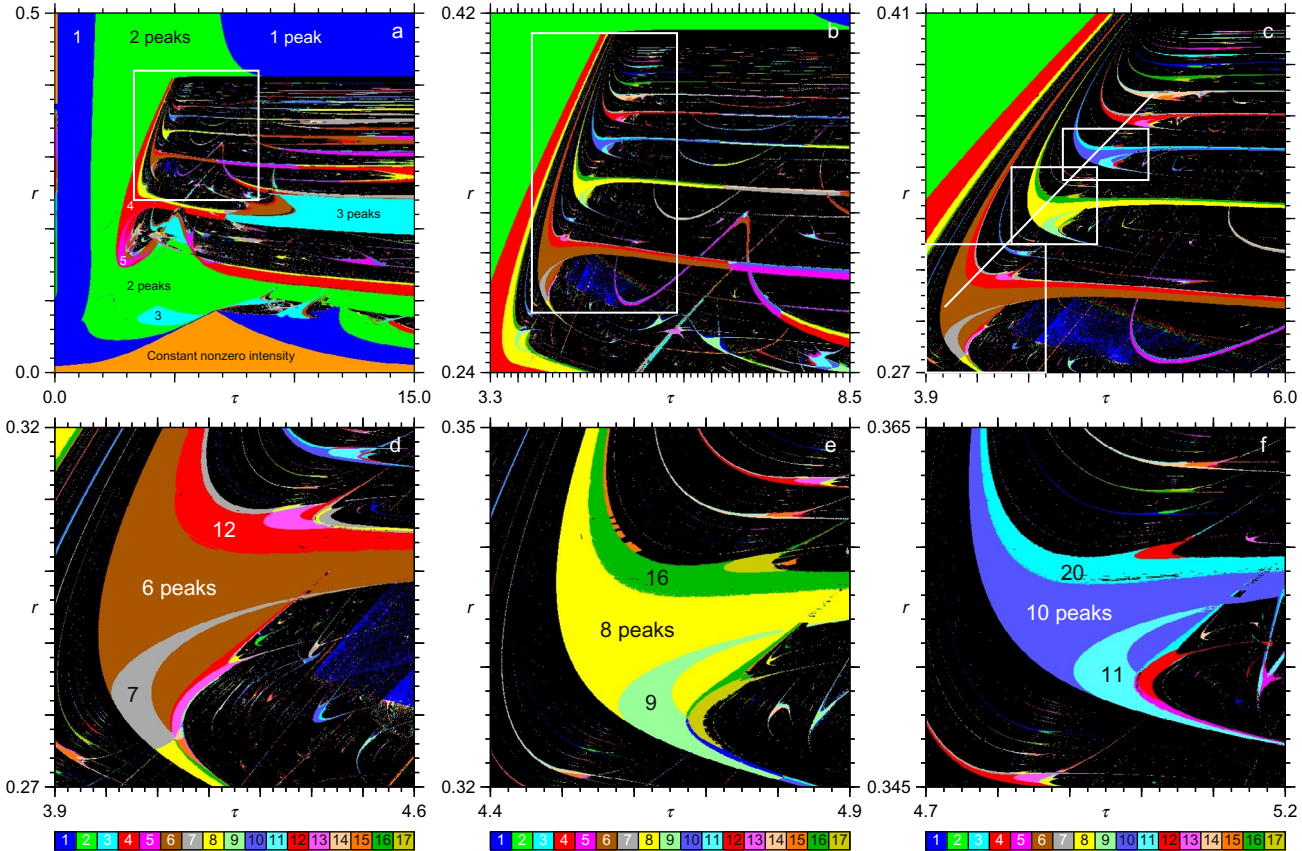


Fig. 25 Parameter windows illustrating the accumulation of stable laser phases on the $\tau \times r$ for $B = 0.25$. Along the line segment in (c), the number of spikes of the laser pulses increases by two as r increases, accumulating on the large window characterized by pulsations with two spikes. In (c) one also recognizes that self-pulsations have a constant number of spikes along the horizontal stripes forming shrimp legs (Façanha et al., 2013; Gallas, 1993; Lorenz, 2008). The bottom row shows that peak doubling and adding occurs *simultaneously* inside the shrimps. Each panel shows 600×600 parameter points.

in Fig. 21. Fig. 25a reveals a number of remarkable facts concerning the self-organization of laser pulsations. For $r \lesssim 0.15$ one essentially finds pulses with either a nonzero constant amplitude or simple periodic oscillations with one peak per period. For r small enough, the laser does not oscillate, independent of the value of the delay. Above $r \simeq 0.15$, complex oscillatory modes become possible, first in small domains for relatively large values of τ , of the order of $\tau \gtrsim 7 \mu\text{s}$.

As r grows, a conspicuous feature observed in Fig. 25a is the large green (gray in the print version) phase which denotes oscillations with two peaks per period. This phase dominates the left side of the stability diagram, together with the black domain representing nonperiodic, “chaotic,” laser modes. Oscillations with larger number of spikes per period become also abundant for $r \gtrsim 1.5$ and $\tau \gtrsim 3 \mu\text{s}$. As indicated in the figure, when r grows in that region one sees what appears to be an abrupt transition from two to five pulses per period. Under further magnification it is possible to realize the existence of a $2 \rightarrow 4$ peak-doubling, then a $4 \rightarrow 5$ adding. The right-hand-side boundary of the 2 peaks green (gray in the print version) phase displays a peak-doubling cascade, as can be seen more clearly from Fig. 25b. Following this doubling cascade there is an alignment of shrimps, namely a sequence of self-similar periodic phases, with complex internal distribution of modes and with number of peaks that grow apparently without bound. Such sequence is shown magnified in Fig. 25c, where a line segment indicates the direction along which the phases accumulate upward when r grows.

The three shrimps inside the boxes in Fig. 25c are magnified in the bottom row. Each panel in Fig. 25d–f displays the number of peaks of the three largest of the infinite number of phases belonging to the shrimps: (6, 12, 7), (8, 16, 9), and (10, 20, 11), respectively. In each shrimp, the number of peaks of the largest region grows by two from shrimp to shrimp when r grows toward the green (gray in the print version) accumulation boundary of two-peaked oscillations. The next two largest regions reveal a remarkable mode unfolding: laser oscillations in the upper regions follow a *peak-doubling* cascade, while oscillations in the lower regions follow a *peak-adding* cascade Junges and Gallas (2012a,b). More complex mode subdivisions are clearly visible, but they are harder to characterize systematically by means other than graphically.

Fig. 26 shows results similar to Fig. 25, but for the $\tau \times B$ control plane. *Mutatis mutandis*, it is not difficult to realize that laser modes self-organize here quite similarly as in the $\tau \times r$ plane. In particular, cascades of peak doublings and additions together, with their accumulations, can be followed with

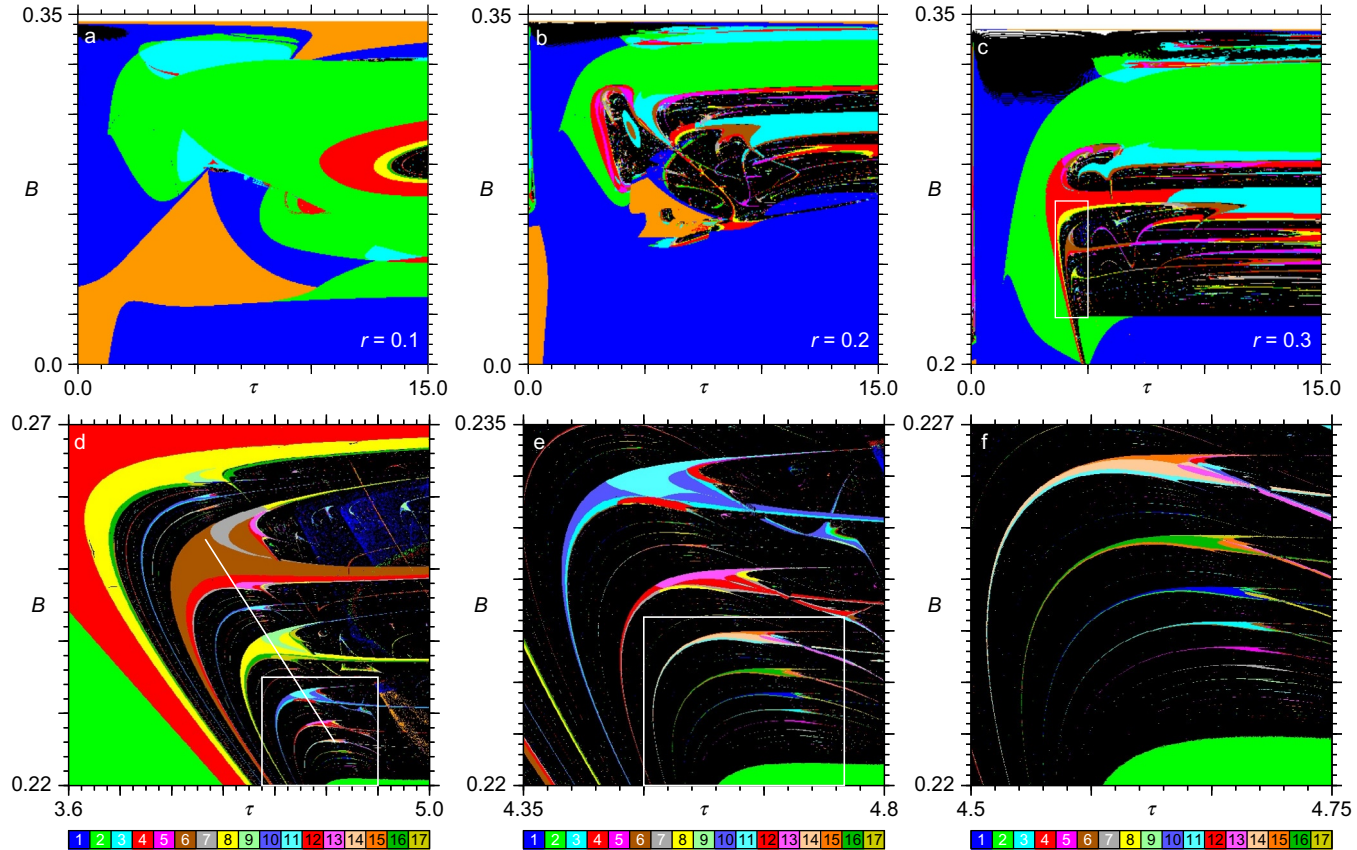


Fig. 26 Top row: Global views of control plane $\tau \times B$ for different values of r . The box in (c) is magnified in (d). Bottom row: Successive magnifications of the box (c), illustrating a typical downwards accumulation cascade of periodic laser modes. In (d), the line segment runs from (4.130, 0.25413) to (4.633, 0.22599). As in Fig. 25, from shrimp to shrimp the number of peaks of the largest phase increases by two peaks via a doublet-adding mechanism (see text). Each panel shows 1200×1200 parameter points.

no difficulty by suitably tuning parameters along the white line in Fig. 26d (from top to bottom), as indicated in the figure.

Fig. 27 presents additional informations concerning the unfolding of oscillatory modes observed along the white lines in Figs. 25c and 26d. In the top row of Fig. 27 one sees bifurcation diagrams depicting local maxima of the laser intensity x recorded along the pair of white lines, defined by the equations

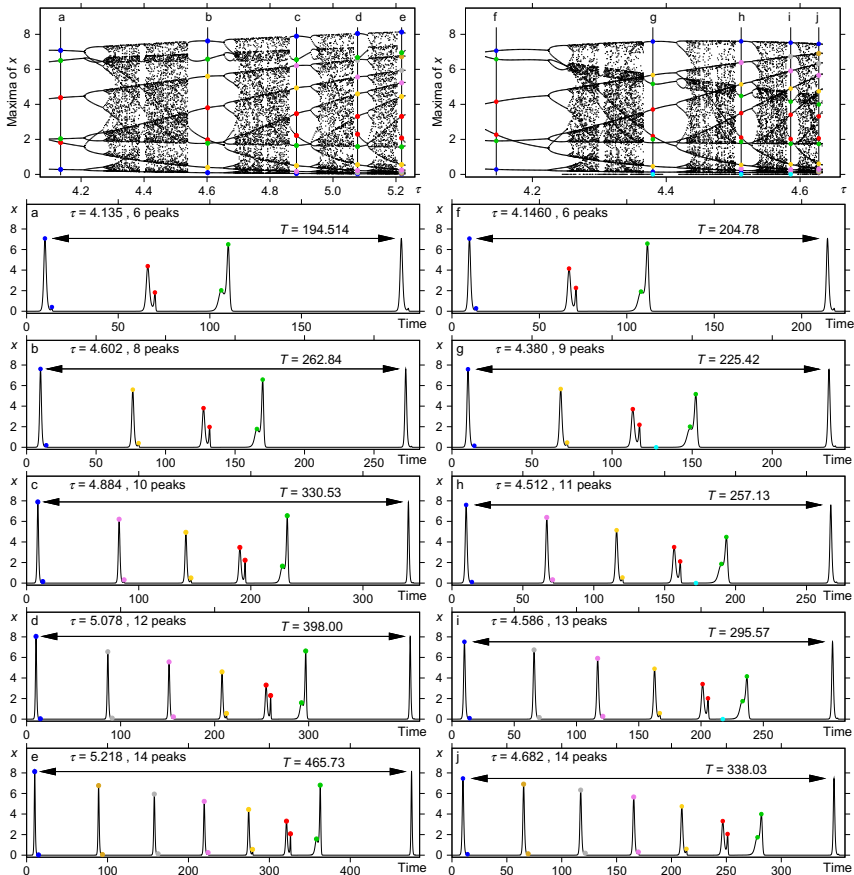


Fig. 27 Top left: Bifurcation diagrams on the $x \times \tau$ plane calculated following the $r(\tau)$ dependence of Eq. (25), namely over the white line (crossing the shrimps) in the $\tau \times r$ diagram of Fig. 25c. (a–e) Temporal evolution $x(t)$ showing laser oscillations near the “center” of the shrimps, marked by vertical lines in the bifurcation diagram. Top right: Bifurcation diagram on the $x \times \tau$ plane calculated following the $B(\tau)$ dependence of Eq. (26), namely over the white line in the $\tau \times B$ diagram of Fig. 26d. (f–j) The corresponding temporal evolutions $x(t)$ at the vertical lines in the bifurcation diagram.

$$r = -0.005705 + 0.073480 \tau, \quad \tau \in [4.0992, 5.2287], \quad (25)$$

$$B = 0.485214 - 0.055952 \tau, \quad \tau \in [4.1300, 4.6330]. \quad (26)$$

Note that to be able to follow the accumulation cascade one must tune two parameters simultaneously. Inside each window of constant number of peaks, the bifurcation diagrams look quite similar in their ordering as well as in the unfolding of the cascade.

Fig. 25d–f manifested clearly the self-similar shrimp nature inside which one finds cascades of peak-doubling and peak-adding. Further, Figs. 25 and 26 revealed that the number of peaks of the phases with largest “volume” increases by two units from shrimp to shrimp. So, a natural question to ask is what sort of changes can laser modes undergo when one proceeds along the cascades? The answer is provided in Fig. 27 which shows the mode evolution along both accumulation cascades. The left column of Fig. 27 refers to the march along the white line in Fig. 25c, namely the line in Eq. (25), while the right column refers to Fig. 26d and to Eq. (26). The top panels in Fig. 27 show bifurcation diagrams for the intervals defined in Eqs. (25) and (26). The bifurcation diagrams contain five vertical lines labeled from (a) to (e), on the left panel, and from (f) to (j), on the right. The parameters corresponding to these vertical lines are located at the center of the shrimps discussed earlier. The temporal evolution for the selected parameters is displayed on the several panels below the bifurcation diagrams.

Fig. 27a–e shows the temporal evolution along the cascade on the $\tau \times r$ control plane. Fig. 27a refers to the first shrimp, where the oscillation shows six peaks per period. This pattern consists of a periodic repetition of three pairs of pulses, indicated by blue (dark gray in the print version), red (gray in the print version), and green (light gray in the print version) dots, each doublet having a small and a big pulse. For convenience, colored dots are also used to identify the branches that they produce in the bifurcation diagram when τ is tuned. The oscillations of the next shrimp, Fig. 27b, have eight peaks per period: the three doublets observed before plus a new doublet marked with yellow (light gray in the print version) dots. Next, Fig. 27c shows 10 peaks per period: the four previous doublets plus a new doublet, marked in violet (light gray in the print version). This addition of peak doublets persists for subsequent shrimps, a new doublet being added to the large peak on the left when moving from shrimp to shrimp. This is illustrated for two additional steps in Fig. 27d and e.

The period T of the oscillations is also recorded in Fig. 27a–e. From them, we obtain a roughly constant increase of the period growth ΔT_i when moving from shrimp to shrimp:

$$\Delta T_1 = 262.84 - 194.51 = 68.33,$$

$$\Delta T_2 = 330.53 - 262.84 = 67.69,$$

$$\Delta T_3 = 398.00 - 330.53 = 67.47,$$

$$\Delta T_4 = 465.73 - 398.00 = 67.73.$$

The temporal evolutions in Fig. 27f–j show that the doublet-adding mechanism is also at work on the $\tau \times B$ control plane. First, note that in Fig. 27d the white line misses the parabolic 7-peaks arc. Thus, generic accumulations occur along slightly curved paths which, however, may be well approximated by straight lines. It also explains why the doublet-adding mechanism starts from Fig. 27g (not from Fig. 27f). More specifically, the difference between the two sequences of temporal evolutions in Fig. 27 is that a new and very small peak appears in Fig. 27g–j, indicated by a light blue (light gray in the print version) dot, due to the fact that, differently from the white line in Fig. 26c, the white line in Fig. 26d now crosses the corresponding shrimps over the region of peak-adding, near the top arm of such structures. Apart from small differences due to the curved path, the unfolding in both columns is the same. On the right column, the increments of the periods are $\Delta T_1 = 257.13 - 225.42 = 31.71$, $\Delta T_2 = 295.57 - 257.13 = 38.44$, $\Delta T_3 = 338.03 - 295.57 = 42.46$. In this case the period is also increasing, but the increments get bigger from shrimp to shrimp. This marked difference should not be difficult to observe in experiments.

It is interesting to note that the above doublet-adding mechanism displayed by the laser mimics a similar mechanism observed by Junges and Gallas (2012b) in a much simpler scenario, involving a single delay-differential equation of a physiological delayed system, the prototypical feedback system introduced by Mackey and Glass to describe a host of physiological disorders, called *dynamical diseases*.



4. CONCLUSIONS AND OUTLOOK

This review described novel and unanticipated physics arising from numerical simulations of a few CO₂ lasers, based on their rate-equation models. We surveyed dynamical features present in two-parameter sections

of their control space and described some of the major regularities observed in them. However, as it is clear from the stability charts presented, the control space is riddled with innumerable features that seem to defy a general classification. The availability of numerically obtained stability charts calls for experiments that should either corroborate them or reveal differences, thereby exposing shortcomings due to the models being used. Knowledge about dynamically rich parameter combinations seen in the stability charts present excellent opportunities for harnessing them into new explorations and applications. The control space of CO₂ lasers remains a very fruitful and convenient test-bed for exploring a plethora of fundamental aspects of nonlinear and chaotic dynamics that only recently became within reach of simulations, thanks to more powerful computer clusters.

We described global regularities of self-pulsations, focusing on the systematic organization of stability domains observed in CO₂ lasers with feedback. Self-pulsations display continuous waveform deformations as parameters are varied. Such deformations create and destroy spikes in oscillatory patterns. Peak creation and destruction result in rich and intricate *isolated* branches appearing and disappearing in bifurcation cascades, a possibility not considered before. As a result of the added flexibility of incorporating an odd number of branches, sequences of branching cascades may emerge in rich combinations of the familiar adding and doubling bifurcations, something that still needs to be better investigated. Branching cascades of spikes result in highly intricate mosaics of periodicity domains in control parameter space as seen, for example, in Figs. 18a and 19.

As may be observed from the bifurcation diagrams in Fig. 27, pulses that form new branches do not show up in a discontinuous manner but arise from peaks that seem to originate from specific bifurcations in windows for lower values of r and that evolve continuously, crossing through domains where chaos predominates, until eventually emerging as extra branches at higher values of r . Furthermore, note that in Fig. 27 the vertical lines were chosen mainly *before* the amplitude where two peaks coincide. By selecting parameters *after* such coincidences, one simply interchanges the order of maxima and minima of the doublets present in Fig. 27a–j.

The dynamics of small pulses following large spikes presents also a number of interesting characteristics worth exploring. For instance, note that the sequence of small pulses following the fundamental one in figures such as Fig. 8b–d decays with a decreasing rate as the coupling r is increased, but the separation between the pulses has roughly the same duration. A simple calculation of the solitary laser equations with zero feedback shows that

the period of the relaxation frequency is of the order of 6 μs and, indeed, corresponds to the period of the decaying relaxation oscillations that follow the main peak. Additionally, as r is increased, it affects the damping of the laser, which decreases. Therefore, the pulsations following the main one are sustained longer. In this context, an interesting open problem is to compute some of the spectra of the time series to characterize the fundamental frequency structures with and without feedback.

We hope that peak-adding cascades not mediated by chaos as well as the discontinuities in the frequency and laser intensity reported here may motivate their experimental corroboration in the near future. A few simple ways of recording experimentally novel phenomena in laser stability diagrams were discussed recently for a semiconductor laser with optoelectronic feedback (Freire and Gallas, 2010; Kovanis et al., 2010). For electronic circuits, some phenomena have already been observed in the laboratory with high resolution (Sack et al., 2013). An interesting related problem with potentially many applications is to investigate systematically the distribution of self-pulsing for laser diodes when acted by delayed feedback and in delay-coupled semiconductor lasers (Junges and Gallas, 2015).

In 1676, Leibniz introduced the expression *aequatio differentialis* to denote a relationship between the two differentials dx and dy associated with a pair of variables x and y . According to Hoffmann (1974), differential equations were at the very origin of Leibniz's work on calculus and were already used by him as early as 1663. Since then, theoretical models of natural phenomena are routinely written in terms of differential equations. The immense utility of differential equations in innumerable branches of natural sciences and its extensive use for over 300 years notwithstanding, they still harbor unanticipated regularities in their control parameter planes that just recently started to be explored and understood. The reason for this immensely late start rests on the proverbial difficulty of solving nonlinear equations analytically and, perhaps more importantly, in the lack until recently of computer clusters performing in the range of several petaflop combined with terabytes of memory. As nicely put by Lorenz (1992), one of the great pioneers of chaos, "Now that computers have become ubiquitous, carefully conceived numerical experiments can enable us to explore a fascinating mathematical world that has not yet opened its doors to classical analytical procedures."

A recent article in *Nature* argues that energy-optimized hybrid computers with a range of processor accuracies should be capable of advancing modeling in fields from climate change to neurosciences (Palmer, 2015). It also states that "high-performance computation is rapidly overtaking

traditional experimentation in many scientific disciplines.” Our paper shows that high-performance computation can considerably help laser optimization in two important practical aspects: first, to pinpoint interesting parameter combinations for more efficient laser operation (chaotic or not) that would be hard to locate by sweeping parameters experimentally and, second, to expose inaccuracies in currently available laser models whenever experimental stability charts are found not to match simulations.

Nowadays, numerical simulations have gone far beyond experiments in parameter space of lasers. Experimental research is especially needed to test the validity of assumptions behind the models in use. One of the appealing features of experimentally determining stability charts is that they will bring a realization of the factors, and of the ignorance we are in as to many of them, needed to improve laser development. If what is predicted is not found in *Nature*, it will still be possible to learn a great deal by asking why not. A number of fruitful innovations resulted from the continued effort during the last four decades to study *chaos* in lasers and other complex systems. However, to understand and classify the organization of *periodicity* is as important an issue as chaos. The technology needed to investigate laser stability charts experimentally exists and the hope is that the younger generation of experimentalists will address such topics in a not so remote future.

ACKNOWLEDGMENTS

I dedicate this work to Prof. Dr. Ricardo Eugenio Francke Sandoval, IF-UFRGS, who in 1975–77 taught Alexandre Lago and myself how to build and apply CO₂ and nitrogen lasers. This work was supported by CNPq, Brazil, by the Deutsche Forschungsgemeinschaft through the Cluster of Excellence *Engineering of Advanced Materials*, and by the Max-Planck Institute for the Physics of Complex Systems, Dresden, in the framework of the *Advanced Study Group on Optical Rare Events*. All bitmaps were computed on the CESUP-UFRGS clusters, located in Porto Alegre, Brazil.

REFERENCES

- Alcantara, P., Guidoni, L., Barsella, A., Fioretti, A., Arimondo, E., 1995. Frequency tuning of homoclinic chaos in an infrared laser with an osmium tetroxide intracavity saturable absorber. *J. Opt. Soc. Am. B* 12, 1326–1333.
- Allaria, E., Arecchi, F.T., Garbo, A.D., Meucci, R., 2001. Synchronization of homoclinic chaos. *Phys. Rev. Lett.* 86, 791.
- Arecchi, F.T., Meucci, R., 2009. Stochastic and coherence resonance in lasers: homoclinic chaos and polarization bistability. *Eur. Phys. J. B* 69, 93–100.
- Arecchi, F.T., Meucci, R., Puccioni, G., Tredicce, J., 1982a. Experimental evidence of subharmonic bifurcations, multistability, and turbulence in a Q-switched gas laser. *Phys. Rev. Lett.* 49, 1217–1219.

- Arecchi, F.T., Meucci, R., Puccioni, G.P., Tredicce, J.R., 1982b. Experimental evidence of subharmonic bifurcations, multistability, and turbulence in a Q-switched gas laser. *Phys. Rev. Lett.* 49, 1217–1219.
- Arecchi, F.T., Lippi, G.L., Puccioni, G.P., Tredicce, J.R., 1984. Deterministic chaos in laser with injected signal. *Opt. Commun.* 51, 308–314.
- Arecchi, F.T., Gadomski, W., Meucci, R., 1986. Generation of chaotic dynamics by feedback on a laser. *Phys. Rev. A* 34, 1617–1620.
- Arecchi, F.T., Meucci, R., Gadomski, W., 1987. Laser dynamics with competing instabilities. *Phys. Rev. Lett.* 58, 2205–2208.
- Arecchi, F.T., Gadomski, W., Meucci, R., Roversi, J.A., 1988. Swept dynamics of a CO₂ laser near threshold: two- versus four-level model. *Opt. Commun.* 65, 47–51.
- Arecchi, F.T., Gadomski, W., Meucci, R., Roversi, J.A., 1989. Delayed bifurcation at the threshold of a swept gain CO₂ laser. *Opt. Commun.* 70, 155–160.
- Arecchi, F.T., Giacomelli, G., Lapucci, A., Meucci, R., 1991. Dynamics of a CO₂ laser with delayed feedback: the short-delay regime. *Phys. Rev. A* 43, 4997–5004.
- Arecchi, F.T., Allaria, E., Leyva, I., 2003. Propensity criterion for networking in an array of coupled chaotic systems. *Phys. Rev. Lett.* 91, 0234101.
- Argyris, J., Faust, G., Haase, M., Friedrich, R., 2015. *An Exploration of Dynamical Systems and Chaos*. Springer, New York.
- Arimondo, E., Casagrande, F., Lugiato, L.A., Glorieux, P., 1983. Repetitive passive Q-switching and bistability in lasers with saturable absorbers. *Appl. Phys. B* 30, 57–77.
- Asquini, M.L., Casagrande, F., 1983. Passive Q-switching in lasers with saturable absorbers: improved treatment of a four-level model. *Nuevo Cimento D* 2, 917–931.
- Barrio, R., Blesa, F., Serrano, S., Shilnikov, A., 2011. Global organization of spiral structures in biparameter space of dissipative systems with Shilnikov saddle-foci. *Phys. Rev. E* 84, 035201.
- Billings, L., Schwartz, I.B., Morgan, D.S., Bolt, E.M., Meucci, R., Allaria, E., 2004. Stochastic bifurcation in a driven laser system: experiment and theory. *Phys. Rev. E* 70, 26220.
- Bonato, C., Gallas, J.A.C., 2007. Accumulation horizons and period adding cascades in optically injected semiconductor lasers. *Phys. Rev. E* 75, 055204(R).
- Bonato, C., Gallas, J.A.C., 2008a. Accumulation boundaries: codimension-two accumulation of accumulations in phase diagrams of semiconductor lasers, electric circuits, atmospheric, and chemical oscillators. *Philos. Trans. R. Soc. A* 366, 505–517.
- Bonato, C., Gallas, J.A.C., 2008b. Periodicity hub and nested spirals in the phase diagram of a simple resistive circuit. *Phys. Rev. Lett.* 101, 054101.
- Bonato, C., Garreau, J.C., Gallas, J.A.C., 2005. Self-similarities in the frequency-amplitude space of a loss-modulated CO₂ laser. *Phys. Rev. Lett.* 95, 143905.
- Brugioni, S., Meucci, R., 2004. Self-focusing effects in a nematic liquid crystal at 10.6 μm . *Eur. Phys. J. D* 28, 277–281.
- Chizhevsky, V.N., 2001. Multistability in dynamical systems induced by periodic perturbations. *Phys. Rev. E* 64, 036223.
- Ciofini, M., Politi, A., Meucci, R., 1993. Effective two-dimensional model for CO₂ lasers. *Phys. Rev. A* 48, 605.
- Ciofini, M., Labate, A., Meucci, R., Galanti, M., 1999. Stabilization of unstable fixed points in the dynamics of a laser with feedback. *Phys. Rev. E* 60, 398–402.
- Dangoisse, D., Glorieux, P., Hennequin, D., 1986. Laser chaotic attractors in crisis. *Phys. Rev. Lett.* 57, 2657–2660.
- Dangoisse, D., Glorieux, P., Hennequin, D., 1987. Chaos in a CO₂ laser with modulated parameters: experiments and numerical simulations. *Phys. Rev. A* 36, 4775–4791.
- Dangoisse, D., Bekkali, A., Papoff, F., Glorieux, P., 1988. Shilnikov dynamics in a passive Q-switching laser. *Europhys. Lett.* 6, 335–340.

- Doedel, E.J., Pando, C.L., 2014. Multiparameter bifurcations and mixed-mode oscillations in Q-switched CO₂ lasers. *Phys. Rev. E* 89, 052904.
- Doedel, E.J., Krauskopf, B., Pando, C.L., 2014. A numerical bifurcation study of a basic model of two coupled lasers with saturable absorption. *Eur. Phys. J. Special Top.* 223, 2847–2856.
- Donati, S., Hwang, S.K., 2012. Chaos and high-level dynamics in coupled lasers and their applications. *Prog. Quant. Electr.* 36, 293–341.
- Duprè, J., Meyer, F., Meyer, C., 1975. Influence des phénomènes de relaxation sur la forme des impulsions fournies par un laser CO₂ déclenché par un absorbant saturable. *Rev. Phys. Appl. (Paris)* 10, 285–294.
- Erneux, T., Glorieux, P., 2010. *Laser Dynamics*. Cambridge University Press, Cambridge.
- Façanha, W., Oldeman, B., Glass, L., 2013. Bifurcation structures in two-dimensional maps: the endoskeletons of shrimps. *Phys. Lett. A* 377, 1264–1268.
- Fox, R.W., Oates, C.W., Hollberg, L., 2001. Stabilizing diode lasers to high finesse cavities. In: van Zee, R.D., Patrick Looney, J. (Eds.), *Experimental Methods in the Physical Sciences, Cavity-Enhanced Spectroscopies*. In: vol. 40. Elsevier, Amsterdam (Chapter 1).
- Freire, J.G., Gallas, J.A.C., 2010. Non-Shilnikov cascades of spikes and hubs in a semiconductor laser with optoelectronic feedback. *Phys. Rev. E* 82, 037202.
- Freire, J.G., Gallas, J.A.C., 2011. Stern-Brocot trees in cascades of mixed-mode oscillations and canards in the extended Bonhoeffer-van der Pol and the FitzHugh-Nagumo models of excitable systems. *Phys. Lett. A* 375, 1097–1103.
- Freire, J.G., Gallas, J.A.C., 2011. Stern-Brocot trees in the periodicity of mixed-mode oscillations. *Phys. Chem. Chem. Phys.* 13, 12191–12198.
- Freire, J.G., Gallas, J.A.C., Field, R.J., 2009. Relative abundance and structure of chaotic behavior: the nonpolynomial Belousov-Zhabotinsky reaction kinetics. *J. Chem. Phys.* 131, 044105.
- Freire, J.G., Pöschel, T., Gallas, J.A.C., 2012. Stern-Brocot trees in spiking and bursting of sigmoidal maps. *Europhys. Lett.* 100, 48002.
- Freire, J.G., Meucci, R., Arecchi, F.T., Gallas, J.A.C., 2015. Self-organization of pulsing and bursting in a CO₂ laser with opto-electronic feedback. *Chaos* 25, 097607.
- Gallas, J.A.C., 1993. Structure of the parameter space of the Hénon map. *Phys. Rev. Lett.* 70, 2714–2717.
- Gallas, J.A.C., 1994. Dissecting shrimps: results for some one-dimensional physical systems. *Physica A* 202, 196–223.
- Gallas, J.A.C., 1995. Structure of the parameter space of a ring cavity. *Appl. Phys. B* 60, S203–S213; *Festschrift Herbert Walther, Supplement issue*.
- Gallas, J.A.C., 2010. The structure of infinite periodic and chaotic hub cascades in phase diagrams of simple autonomous systems. *Int. J. Bifurc. Chaos* 20, 197–211.
- Gallas, J.A.C., 2015. Periodic oscillations of the forced Brusselator. *Mod. Phys. Lett. B* 29, 1530018.
- Gallas, J.A.C., Nusse, H.E., 1996. Periodicity versus chaos in the dynamics of cobweb models. *J. Econ. Behav. Org.* 29, 447–464.
- Gallas, M.R., Gallas, M.R., Gallas, J.A.C., 2014. Distribution of chaos and periodic spikes in a three-cell population model of cancer. *Eur. Phys. J. Special Top.* 223, 2131–2144.
- Gilmore, R., 1998. Topological analysis of chaotic dynamical systems. *Rev. Mod. Phys.* 70, 1455–1529.
- Gilmore, R., Lefranc, M., 2002. *The Topology of Chaos, Alice in Stretch and Squeeze Land*. Wiley, New York.
- Goswami, B.K., 1994. Analytical studies on the period doubling bifurcations from the harmonic solutions of the parameter modulated single mode two-level laser. *Phys. Lett. A* 190, 279–284.

- Hauser, M.J.B., Gallas, J.A.C., 2014. Nonchaos-mediated mixed-mode oscillations in an enzyme reaction system. *J. Phys. Chem. Lett.* 5, 4187–4193.
- Hilborn, R.C., 2000. *Chaos and Nonlinear Dynamics: An Introduction for Scientists and Engineers*, second ed. Oxford University Press, Oxford.
- Hoff, A., da Silva, D.T., Manchein, C., Albuquerque, H.A., 2014. Bifurcation structures and transient chaos in a four-dimensional Chua model. *Phys. Lett. A* 378, 171–177.
- Hoffmann, J.E., 1974. *Leibniz in Paris 1672–1676*. Cambridge University Press, Cambridge.
- Hunt, B.R., Gallas, J.A.C., Grebogi, C., Yorke, J.A., Koçak, H., 1999. Bifurcation rigidity. *Physica D* 129, 35–56.
- Junges, L., Gallas, J.A.C., 2012a. Frequency and peak discontinuities observed in self-pulsations of a CO₂ laser with feedback. *Opt. Commun.* 285, 4500–4506.
- Junges, L., Gallas, J.A.C., 2012b. Intricate routes to chaos in the Mackey–Glass delayed feedback system. *Phys. Lett. A* 376, 2109–2116.
- Junges, L., Gallas, J.A.C., 2015. Stability diagrams for continuous wide-range control of two mutually delay-coupled semiconductor lasers. *New J. Phys.* 17, 053038.
- Junges, L., Gallas, J.A.C., 2016. Impact of delayed feedback of arbitrary duration in self-pulsations of a CO₂ laser. *J. Opt. Soc. Am. B* 33, 373.
- Junges, L., Pöschel, T., Gallas, J.A.C., 2013. Characterization of the stability of semiconductor lasers with delayed feedback according to the Lang–Kobayashi model. *Eur. Phys. J. D* 67, 149.
- Kane, D.M., Shore, K.A., 2005. *Unlocking Dynamical Diversity: Optical Feedback Effects on Semiconductor Lasers*. Wiley, New York.
- Kovanis, V., Gavrielides, A., Gallas, J.A.C., 2010. Labyrinth bifurcations in optically injected diode lasers. *Eur. Phys. J. D* 58, 181–186.
- Larson, L.E., Liu, J.M., Tsimring, T.S., 2006. *Digital Communications Using Chaos and Nonlinear Dynamics*. Springer, New York.
- Lefranc, M., Glorieux, P., 1993. Topological analysis of chaotic signals from a CO₂ laser with modulated losses. *Int. J. Bifur. Chaos* 3, 643–650.
- Lefranc, M., Hennequin, D., Glorieux, P., 1992. Improved correlation dimension estimates through change of variable. *Phys. Lett. A* 163, 269–274.
- Leyva, I., Allaria, E., Boccaletti, S., Arecchi, F.T., 2003. Competition of synchronization domains in arrays of chaotic homoclinic systems. *Phys. Rev. E* 68, 066209.
- Liu, Y., de Oliveira, P.C., Danailov, M.B., Leite, J.R.R., 1994. Chaotic and periodic passive Q switching in coupled CO₂ lasers with a saturable absorber. *Phys. Rev. A* 50, 3464–3470.
- Lorenz, E.N., 1992. The slow manifold—what is it? *J. Atmos. Sci.* 49, 2449–2451.
- Lorenz, E.N., 2008. Compound windows of the Hénon map. *Physica D* 237, 1689–1704.
- Mandel, P., Erneux, T., 2003. Propensity criterion for networking in an array of coupled chaotic systems. *Phys. Rev. Lett.* 91, 234101.
- Meucci, R., Ciofini, M., Wang, P.Y., 1992. Analysis of the dynamical behavior of a Q-switched CO₂ laser: the linear and the nonlinear regime. *Opt. Commun.* 91, 444–452.
- Meucci, R., Labate, A., Ciofini, M., 1997. Controlling chaos by negative feedback of subharmonic components. *Phys. Rev. E* 56, 2829–2834.
- Meucci, R., Cinotti, D., Allaria, E., Billings, L., Triandaf, I., Morgan, D., Schwartz, I.B., 2004. Global manifold control in a driven laser: sustaining chaos and regular dynamics. *Physica D* 189, 70–80.
- Ohtsubo, J., 2013. *Semiconductor Lasers: Stability, Instability and Chaos*. Springer, Berlin.
- Oliveira, D.F.M., Leonel, E.D., 2011. Parameter-space for a dissipative Fermi–Ulam model. *New J. Phys.* 13, 123012.
- Oppo, G.L., Politi, A., 1985. Toda potential in laser equations. *Z. Phys. B* 59, 111.
- Ott, E., 2002. *Chaos in Dynamical Systems*. Cambridge University Press, Cambridge.
- Palmer, T., 2015. Build imprecise supercomputers. *Nature* 526, 32–33.

- Pando, C.L., Meucci, R., Ciofini, M., Arecchi, F.T., 1993. CO₂ laser with modulated losses: theoretical models and experiments in the chaotic regime. *Chaos* 3, 279–286.
- Pando, C.L., Luna Acosta, G.A., Meucci, R., Ciofini, M., 1995. Highly dissipative Hénon map behavior in the four-level model of the CO₂ laser with modulated losses. *Phys. Lett. A* 199, 191–198.
- Patel, C.K.N., 1964. Continuous-wave laser action on vibrational-rotational transitions of CO₂. *Phys. Rev.* 136, 1187–1193.
- Picozzi, A., Hansson, J.G.T., Suret, P., Randoux, S., Millot, G., Christodoulides, D.N., 2014. Optical wave turbulence: towards a unified nonequilibrium thermodynamic formulation of statistical nonlinear optics. *Phys. Rep.* 542, 1–132.
- Pisarchik, A.N., Kuntsevich, B.F., 2001. Nonlinear dynamics of a CO₂ laser with current modulation and cavity detuning. *J. Opt. B Quantum Semiclass. Opt.* 3, 363–371.
- Pisarchik, A.N., Meucci, R., Arecchi, F.T., 2001. Theoretical and experimental study of discrete behavior of Shilnikov chaos in a CO₂ laser. *Eur. Phys. J. D* 13, 385–391.
- Sack, A., Freire, J.G., Lindberg, E., Pöschel, T., Gallas, J.A.C., 2013. Discontinuous spirals of stable periodic oscillations. *Sci. Rep.* 3, 3350.
- Sciamanna, M., Shore, K.A., 2015. Physics and applications of laser diode chaos. *Nat. Photon.* 9, 151–162.
- Strogatz, S., 2015. *Nonlinear Dynamics and Chaos with Applications to Physics, Biology, Chemistry, and Engineering*. Westview Press, Boulder.
- Susa, S.I., Erneux, T., Barsella, A., Lepers, C., Dangoisse, D., Glorieux, P., 2002. Synchronization through bursting oscillations for two coupled lasers. *Phys. Rev. A* 63, 013815.
- Tachikawa, M., Hong, F.L., Tanii, K., Shimizu, T., 1988. Deterministic chaos in passive Q-switching pulsation of a CO₂ laser with saturable absorber. *Phys. Rev. Lett.* 60, 2266–2268.
- Tredicce, J.R., Arecchi, F.T., Puccioni, G.P., Poggi, A., Gadomski, W., 1986. Dynamic behavior and onset of low-dimensional chaos in a modulated homogeneously broadened single-node laser: experiments and theory. *Phys. Rev. A* 34, 2073–2081.
- Uchida, A., Rogister, F., Garcia-Ojalvo, J., Roy, R., 2005. Synchronization and communication with chaotic laser systems. In: Wolf, E. (Ed.), *Progress in Optics*, vol. 48. Elsevier, Dordrecht.
- Vandermeiren, W., Stiens, J., Shkerdin, G., Vounckx, R., 2012. Theoretical analysis of partial-spatial Q-switching dynamics using a two-level CO₂ laser model. *IEEE J. Quant. Electron.* 48, 447–453.
- Varone, A., Politi, A., Ciofini, M., 1995. CO₂ laser dynamics with feedback. *Phys. Rev. A* 52, 3176–3182.
- Vitolo, R., Glendinning, P., Gallas, J.A.C., 2011. Global structure of periodicity hubs in Lyapunov phase diagrams of dissipative flows. *Phys. Rev. E* 84, 016216.
- Wang, P., Lapucci, A., Meucci, R., Arecchi, F.T., 1990. Onset of subcritical bifurcation in a CO₂ laser with feedback. *Opt. Commun.* 80, 42–46.
- Wieczorek, S., Krauskopf, B., Simpson, T.B., Lenstra, D., 2005. The dynamical complexity of optically injected semiconductor lasers. *Phys. Rep.* 416, 1–128.
- Yang, Q.S., Wang, P.Y., Yin, H.W., Dai, J.H., Zhang, H.J., 1997. Global stability and oscillation properties of a two-level model for a class B laser with feedback. *Opt. Commun.* 138, 325–329.
- Zehnlé, V., Dangoisse, D., P. Glorieux, 1992. Behavior of a CO₂ laser under loss modulation: critical analysis of different theoretical models. *Opt. Commun.* 90, 99–105.
- Zeni, A.R., Gallas, J.A.C., Fioretti, A., Papoff, F., Zambon, B., Arimondo, E., 1993. Lyapunov exponents and return maps for a model of a laser with saturable absorber. *Phys. Lett. A* 172, 247–255.
- Zinth, W., Laubereau, A., Kaiser, W., 2011. The long journey to the laser and its rapid development after 1960. *Eur. Phys. J. H* 36, 153–181.